J. Fluid Mech. (2003), *vol.* 494, *pp.* 319–353.
DOI: 10.1017/S0022112003006189 Printed in the United Kingdom

The dynamics of breaking progressive interfacial waves

By OLIVER B. FRINGER AND ROBERT L. STREET

Department of Civil and Environmental Engineering, Stanford University, Stanford, CA 94305-4020, USA

(Received 27 January 2003 and in revised form 23 June 2003)

Two- and three-dimensional numerical simulations are performed to study interfacial waves in a periodic domain by imposing a source term in the horizontal momentum equation. Removing the source term before breaking generates a stable interfacial wave. Continued forcing results in a two-dimensional shear instability for waves with thinner interfaces, and a convective instability for waves with thick interfaces. The subsequent three-dimensional dynamics and mixing is dominated by secondary cross-stream convective rolls which account for roughly half of the total dissipation of wave energy. Dissipation and mixing are maximized when the interface thickness is roughly the same size as the amplitude of the wave, while the mixing efficiency is a weak function of the interface thickness. The maximum instantaneous mixing efficiency is found to be 0.36 ± 0.02.

1. Introduction

Breaking internal waves are responsible for a significant portion of mixing of heat, salt and nutrients throughout much of the world's oceans. According to Munk & Wunsch (1998): 'Without deep mixing, the ocean would turn, within a few thousand years, into a stagnant pool of cold, salty water . . .'

Based on a balance between mixing and deep-water upwelling, the average eddy diffusivity of the ocean is roughly $10^{-4}\,\mathrm{m^2\,s^{-1}}$. Despite this prediction, Munk & Wunsch (1998) report that profiler measurements in the ocean away from boundaries yield diffusivities of the order of $10^{-5}\,\mathrm{m^2\,s^{-1}}$. One possible explanation of this dichotomy is that the eddy diffusivity is very large in small localized turbulent patches over a small percentage of the ocean. The most likely source for this elevated diffusivity is internal wave breaking.

Measurements reveal clear signatures of large-amplitude internal waves. For example, the measurements of Stanton & Ostrovsky (1998) reveal a pronounced signature of solitary internal waves propagating along the thermocline off the coast of Oregon. Their results provide evidence to the existence of internal waves of extremely large amplitude that propagate in the littoral ocean. Petruncio, Rosenfeld & Paduan (1998) cite observations of internal wave amplitudes of 60–120 m in depths ranging from 120 to 220 m in Monterey Bay. These waves are believed to propagate in some nonlinear fashion in which they ultimately end up breaking. Rosenfeld & Kunze (1998) provide evidence for this hypothesis in their internal wave measurements in Monterey Canyon, where they show that there is a peak in the $M6$ internal tide component that is 10% in magnitude of the $M2$ component. This indicates a strong nonlinear cascade toward higher frequencies that is probably due to internal wave

breaking. However, this cascade is so intermittent and sparse that it is difficult to measure actual breaking events in the ocean. Large-scale ocean models cannot feasibly capture such small-scale events, so they must be parameterized through some diffusivity based on local flow variables. These parameterizations require a detailed understanding of the mechanisms that lead to and follow a breaking event.

Of particular interest in the study of breaking progressive interfacial waves is a determination of the initial instability that leads to breaking. In their experiments on breaking interfacial waves on a slope, Michallet & Ivey (1999) show that the initial instability leading to breaking is convective. That is, the maximum fluid velocity u_{max} within the wave exceeds the wave speed c, and a convective instability occurs when the heavier lower layer fluid overlies the lighter layer fluid. This same mechanism is what leads to breaking for surface waves at and away from boundaries. Away from boundaries, progressive surface waves break owing to a convective instability when the angle of the crest reaches 120° (Stokes 1880). The situation is not as clear for progressive interfacial waves away from boundaries. While the fluid velocity within the wave increases with increasing steepness, so does the shear that occurs at the interface between the two layers. As a result, both a convective instability and a shear instability are likely to occur. In their fifth-order expansion of deep-water interfacial wave properties in the steepness ka, where $k = 2\pi/L$ is the wavenumber and a is the wave amplitude, Tsugi & Nagata (1973) hypothesize that shear instabilities occur before the fluid velocity exceeds the wave speed, indicating that a shear instability results before a convective instability for large-amplitude interfacial waves. Holyer (1979), on the other hand, calculates the maximum steepness of an irrotational Boussinesq interfacial wave numerically to thirty-first order in the steepness ka and shows that $u_{max} > c$ when $ka = 1.1$. Clearly, the only condition that will limit a breaking interfacial wave in an irrotational computation is a convective instablity. This same result is also obtained by Meiron & Saffman (1983), who compute the critical steepness for overhanging interfacial gravity waves. Thorpe (1978) studies the behaviour of progressive interfacial waves with and without the presence of mean shear using asymptotic expansions as well as laboratory experiments. To third order in ka without shear, his calculations and experiments show that $u > c$ beneath the crest when $ka = 0.33$, which is substantially lower than the value of $ka = 1.1$ calculated by Holyer (1979). This discrepancy results from Thorpe's calculations involving a lower depth that is 1/3 the depth of the upper layer, unlike the calculations of Holyer (1979) which were performed for infinite layer depths.

The ambiguous nature of what governs the initial instability for breaking progressive interfacial waves away from boundaries also exists in the study of breaking internal waves away from boundaries in critical layers. In their two-dimensional direct numerical simulations, Winters & D'Asaro (1989) show that intensified wave shear near the critical level leads to a shear instability, despite the appearance of statically unstable density gradients. Winters & Riley (1992) later confirm this two-dimensional behaviour in their stability analysis using the Taylor–Goldstein equation (Drazin 1977) with approximate velocity and density fields that closely represent those in a critical layer. While they show that the predominant instability resulting from streamwise perturbations is one of shear, which actually supresses two-dimensional convective instabilities, they show that spanwise perturbations result in a convective instability. Lin *et al.* (1993) use a similar procedure, but instead use the actual velocity and density fields from their two-dimensional direct numerical simulations as the velocity and density fields in the Taylor–Goldstein equation. After applying Squire's theorem to the flow, they conclude that a three-dimensional study would be required

to confirm the nature of the most unstable cross-stream instability, which is convective. Likewise, Dörnbrack & Gerz (1995) cite from their two-dimensional simulations of a critical level that most of the energy is contained in convectively driven cores that are naturally three-dimensional, but are being inhibited by the two-dimensional nature of the simulation. Using three-dimensional simulations, Winters & D'Asaro (1994) show that the dominant instability is clearly a three-dimensional convective instability that results in spanwise convective rolls, which is confirmed by the three-dimensional simulations of critical layers in a shear flow over a wavy bed of Dörnbrack (1998), who also finds that the dominant instability is convective. Both papers find that a three-dimensional convective mixing layer develops just below (or above) the critical level that develops in conjunction with spanwise rolls associated with Rayleigh–Taylor convective instabilities. The mixing layer develops a slight distance away from the critical level as a result of the nonlinear transfer of wave energy to the mean flow, which effectively moves the critical level toward the wave source.

Along with a determination of the initial instability, of critical importance in the understanding of the dynamics of breaking progressive interfacial waves is the mixing efficiency of the breaking process. During a turbulent event in a stratified flow, at the same time energy is converted irreversibly into heat owing to viscous dissipation, energy is also converted irreversibly into mixing of the background density field. How efficiently energy is converted into mixing the background density field is termed the mixing efficiency. The maximum theoretical mixing efficiency is that of a Rayleigh–Taylor instability, in which 50% of the total energy lost is converted into background potential energy (Linden & Redondo 1991). From first principles, McEwan (1983*a*) shows that the mixing efficiency must lie in the neighbourhood of 0.25–0.50, and depends on the ratio L_c/δ, where L_c is the initial displacement of a fluid particle perturbed from its rest state, and δ is the final thickness of the mixed layer. Thompson (1980) shows that the mixing efficiency is given by $\eta = Ri$, where Ri is the gradient Richardson number of the flow. Because a pure Kelvin–Helmholtz instability results when $Ri < 1/4$, the generally accepted quantity of the mixing efficiency for shear-induced events is 0.25. Ivey & Imberger (1991) define a flux Richardson number R_f, in which the mixing efficiency is given by the ratio of the buoyancy flux to the net available turbulent mechanical energy. They show that for shear flows in fluids with a Prandtl number greater than 1, R_f peaks at 0.2.

Laboratory and numerical experiments of breaking internal waves arrive at mixing efficiencies varying from 0.13 to 0.38. To our knowledge, the only computation of the mixing efficiency of a breaking interfacial wave is that computed experimentally for breaking interfacial waves on slopes by Michallet & Ivey (1999), which peaks at 0.25. In his continuously stratified standing-wave experiments, McEwan (1983*a*) generates finite-amplitude internal waves with a paddle in a square tank, and computes an average mixing efficiency of 0.26 ± 0.06. Lin *et al.* (1993) estimate the mixing efficiency for a critical layer of 1/6 for the two-dimensional case and 1/8 for the three-dimensional case. They hypothesize that these approximations are rather high, since their model lacks significant resolution, which indicates that a dominant component of the mixing results from numerical diffusion. In his simulations of critical layers, Dörnbrack (1998) computes a mixing efficiency of roughly 0.2. The largest value of the mixing efficiency is that computed for internal waves on critically sloped topography by Slinn & Riley (1998*a*, *b*). In their numerical simulations, they compute mixing efficiencies of between 0.32 and 0.38.

Breaking interfacial waves are akin to breaking free-surface waves in many respects. However, the computational issues associated with each are substantially different.

Turbulent free-surface simulations that do not involve breaking map the domain onto one that follows the surface with the use of a ζ-coordinate system, such as the large-eddy simulation of nonlinear free-surface waves of Hodges & Street (1999). When capturing the breaking physics is desired, it is necessary to keep track of the complex interface and, in some cases, compute the surface tension if the Bond number is low enough. Most notable of these methods is the marker and cell technique developed by Harlow & Welch (1965), or the interface tracking method of Puckett *et al.* (1997). One of the very few Navier–Stokes simulations of Boussinesq interfacial waves in the literature is presented by Chen *et al.* (1999) as a test case in the implementation of the volume of fluid (VOF) method to simulate breaking free-surface waves. They simulate an interfacial wave by setting the density ratio between the upper and lower layers to 0.01, but only to test the ability of the code to match the correct attenuation. As with all VOF methods, mixing across the interface cannot be computed.

In this paper we employ two- and three-dimensional direct numerical simulations to answer two fundamental questions associated with breaking progressive interfacial waves away from boundaries that have not been addressed in the literature. First, because the findings with regard to breaking interfacial waves have been ambiguous, we determine the critical amplitude of breaking progressive interfacial waves and the associated limiting instability. Secondly, we compute the mixing efficiency of the breaking process and analyse the three-dimensional structure of the ensuing turbulence.

2. Governing equations and numerical method

The forced Boussinesq equations of motion with constant kinematic viscosity are given by

$$\frac{\partial u_i}{\partial t} + \frac{\partial}{\partial x_j}(u_i u_j) = -\frac{1}{\rho_0}\frac{\partial p}{\partial x_i} + \nu\frac{\partial^2 u_i}{\partial x_j \partial x_j} - \frac{g}{\rho_0}(\rho - \rho_r)\,\delta_{i3} + F\delta_{i1}, \tag{2.1}$$

subject to the continuity constraint

$$\frac{\partial u_i}{\partial x_i} = 0, \tag{2.2}$$

where the density field evolves according to

$$\frac{\partial \rho}{\partial t} + \frac{\partial}{\partial x_j}(\rho u_j) = \kappa\frac{\partial^2 \rho}{\partial x_j \partial x_j}, \tag{2.3}$$

and the interfacial wave forcing function F is defined in § 3.1. The Einstein summation convention is assumed with $i, j = 1, 2, 3$ and x_3 is the vertical coordinate. Here, ν is the kinematic viscosity of water and κ is the thermal diffusivity of heat in water. It is assumed that the pressure field represents a departure from some arbitrary hydrostatic reference state. If p_T represents the total pressure, then it is related to the pressure in equation (2.1) via

$$p_T(x, y, z, t) = p(x, y, z, t) + p_r(z), \tag{2.4}$$

where $p_r(z)$ is the reference pressure field and is related to the reference density field $\rho_r(z)$ by

$$\frac{\partial p_r(z)}{\partial z} = -\rho_r(z)g. \tag{2.5}$$

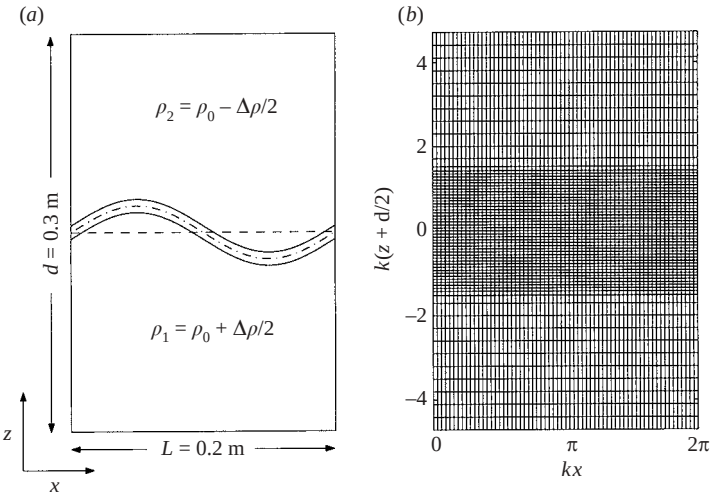

FIGURE 1. (*a*) Physical and (*b*) computational set-up of the domain used to study breaking interfacial waves. The density difference is $\Delta\rho/\rho_0 = 0.03$ and the upper and lower boundaries are free-slip, while the lateral boundaries are periodic. Every fourth grid cell is plotted in (*b*) for clarity. Waves propagate from left to right.

This substitution is useful for computations of stratified flows in which the solution is started from rest, for which the reference pressure field is taken as the initial hydrostatic pressure field.

The numerical discretization of the momentum equations is similar to that carried out by Zang, Street & Koseff (1994), except the pressure correction method (Armfield & Street 2000) is employed to obtain second-order accuracy in time. In the work of Zang, Street & Koseff (1994), the diffusive terms are discretized with a Crank–Nicholson scheme and all other terms are left explicit with the second-order Adams–Bashforth scheme. Momentum is advected with the QUICK scheme of Leonard (1979). During wave growth, scalar advection is computed with a background potential energy preserving scheme (Fringer 2003) which maintains the background potential energy during wave growth. When wave breaking begins, scalar advection is computed with the SHARP scheme (Leonard 1987). The discrete momentum and transport equations are solved using approximate factorization and the pressure Poisson equation is solved with the multigrid method.

3. Simulation set-up

3.1. *Generating interfacial waves*

We study interfacial waves in the periodic domains of width W and depth d shown in figures 1 and 2. The interfacial waves have a wavelength L, wavenumber $k = 2\pi/L$, amplitude a, and interface thickness δ, defined by

$$\rho(z = -d/2 - \delta/2) - \rho(z = -d/2 + \delta/2) = \alpha\Delta\rho, \tag{3.1}$$

where z is measured positive upwards from the top of the domain, $\alpha = 0.99$, and the density difference between the two layers is $\Delta\rho/\rho_0 = 0.03$, where $\rho_0 = 1000\,\mathrm{kg\,m^{-3}}$ is the reference density. We refer to the steepness of the waves as ka and the non-dimensional interface thickness of the waves as $k\delta$. Prior to application of the forcing function, the initial velocity field is quiescent and the initial density field is

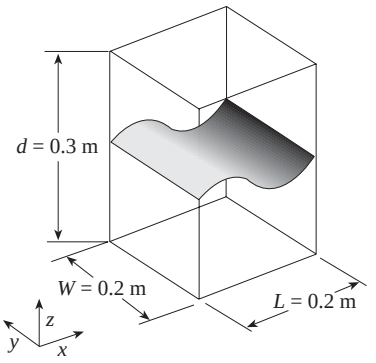

FIGURE 2. Three-dimensional domain, showing the initial interface taken from the two-dimensional simluations. The wave propagates from left to right.

given by

$$\frac{\rho}{\rho_0}(z) = -\frac{\Delta\rho}{2\rho_0}\tanh\left[\frac{2(kz+kd/2)}{k\delta}\tanh^{-1}(\alpha)\right]. \tag{3.2}$$

The linearized wave frequency ω for small ka for interfacial waves with this non-zero $k\delta$ density profile is computed using the modal analysis of the Appendix. The associated non-zero interface thickness wave period is given by $T = 2\pi/\omega$. In the limit of an infinitessimally thin interface thickness ($k\delta \to 0$), the associated frequency and period are given by $\omega_0^2 = g'k/2$ and $T_0 = 2\pi/\omega_0$, where $g' = g\Delta\rho/\rho_0$ is the reduced gravity.

Following the method of forcing surface waves with a momentum source in the form of a free-surface pressure (Baker, Meiron & Orszag 1982), we impose a two-dimensional source term in the horizontal momentum equation that follows the interfacial wave according to

$$F(x,z,t) = F_0 f(t) R_f(x,z,t)\sin(kx - kx_z(t)), \tag{3.3}$$

where F_0 is the magnitude of the forcing function and the interface midpoint, defined by $x_z(t)$, moves in the positive direction at the wave speed c. This point is determined numerically by computing the point in space at which the interface $\zeta(x,t)$, defined by $\rho(x, z=\zeta, t) = 0$, crosses the mid-depth line defined by $z = -d/2$. Because the waves are forced until breaking occurs, we employ a quarter-cosine function in which the magnitude of the forcing function tapers off just before breaking. This transient function $f(t)$ is given by

$$f(t) = \begin{cases} 1, & t < t_f, \\ \frac{1}{2}\left[1 + \cos\left(\frac{1}{2}\omega(t - t_f)\right)\right], & t_f < t < t_f + \dfrac{2\pi}{\omega}, \\ 0, & t > t_f + \dfrac{2\pi}{\omega}, \end{cases} \tag{3.4}$$

where t_f is the desired time at which the forcing function begins to decay. The function $R_f(x,z,t)$ is an approximation to the first mode horizontal velocity profile of the interfacial wave field, and is given by

$$R_f(x,z,t) = -\frac{2\rho(x,z,t)}{\Delta\rho}\exp(-k|z + d/2 - \zeta(x,t)|), \tag{3.5}$$

where $\rho(x,z,t)$ is the two-dimensional density field as it evolves in time.

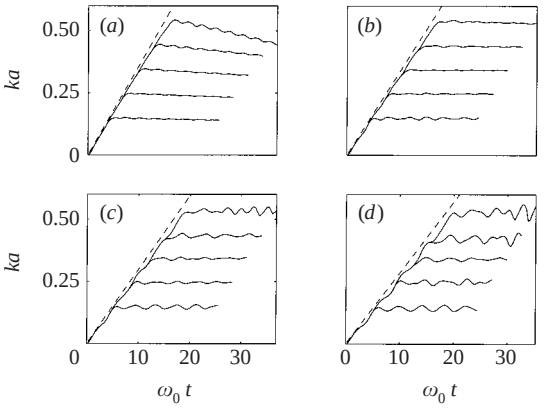

FIGURE 3. Steepness ka as a function of non-dimensional time $\omega_0 t$ for waves with different interface thickness $k\delta$ forced with the forcing function in equation (3.3). The solid lines are from the numerical simulations and the dashed line is from equation (3.9). (*a*) $k\delta = \pi/10$; (*b*) $3\pi/10$; (*c*) $\pi/2$; (*d*) $7\pi/10$.

Applying the forcing function (3.3) to the Boussinesq equations, (2.1), generates a nonlinear interfacial wave that grows with a density field that is closely approximated by

$$\frac{\rho}{\rho_0}(x, z, t) = -\frac{\Delta\rho}{2\rho_0} \tanh\left[\frac{2(kz + kd/2 - k\zeta(x, t))}{k\delta} \tanh^{-1}(\alpha)\right], \tag{3.6}$$

where the interface ζ is given by

$$k\zeta(x, t) = ka(t)\cos(kx - kx_z(t)), \tag{3.7}$$

and $ka(t)$ is the steepness as a function of time. Tsugi & Nagata (1973) show that the fifth-order expansion of the interface in powers of ka deviates very little from this approximation even for large ka. In its most simple form, the forced horizontal momentum equation can be written as

$$\frac{\partial u_{max}}{\partial t} = F_0, \tag{3.8}$$

where u_{max} is the maximum horizontal velocity within the interfacial wave, and is given to first order in the steepness ka as $u_{max} = a\omega$. Substitution into (3.8) yields the steepness as a function of time as

$$ka(t) = 2\left(\frac{F_0}{g'}\right)\left(\frac{\omega_0}{\omega}\right)\omega_0 t. \tag{3.9}$$

This result is compared to results of actual forced interfacial waves in the next section.

3.2. *Applying the forcing function to two- and three-dimensional simulations*

To simulate interfacial waves, we apply the forcing function (3.3) to the interfacial wave field in the domain shown in figure 1 on a 256^2 finite-volume two-dimensional grid and use $F_0/g' = 0.034$ for all of the simulations ($F_0 = 0.01\,\mathrm{m^2\,s^{-1}}$). Figure 3 depicts the steepness as a function of time for non-breaking waves of different interface thickness $k\delta$ when forced with increasing release times t_f. Increasing the release time t_f produces stable waves with increasing steepnesses that closely follow the steepness relation given in equation (3.9). Although this relationship is only accurate to first order in ka, it yields surprisingly good agreement for large ka. The

steepness decays more for the thinner interface waves once the forcing is removed, while the oscillations increase for the thicker interface waves after forcing removal. This attests to the degredation of the effectiveness of the forcing function as the interface thickness becomes very large. However, these post-release effects are not relevant for the present simulations because breaking occurs during forcing and before transient effects can alter the wave dynamics.

Continuous application of the forcing function eventually leads to breaking at a breaking time t_b and critical steepness ka_c, as determined in § 4.1. Using this knowledge of t_b, two-dimensional breaking dynamics are analysed by forcing interfacial waves with the release time in equation (3.4) given by $t_f = t_b - T/2$. This guarantees that the forcing function does not continue to add energy to the flow and alter the dynamics once breaking begins.

For the three-dimensional simulations, the 256^2 two-dimensional results at $t = t_b - T/2$ are interpolated onto the 128^3 three-dimensional domain shown in figure 2 and the forcing is ramped down over one wave period as specified in equation (3.4). This saves on unnecessary three-dimensional computation time since the two- and three-dimensional pre-breaking simulations are identical. The initial conditions for the three-dimensional computations are perturbed with

$$u_1^+(x, y, z) = (1 + \alpha R)u_1^-(x, z),$$
$$u_3^+(x, y, z) = (1 + \alpha R)u_3^-(x, z),$$

where $R \in \{-1, 1\}$ is a uniformly distributed random number, $\alpha = 10^{-2}$ is the scale factor, and the $-$ and $+$ superscripts are used to indicate the solutions just before and just after perturbation, respectively. In two dimensions, no white noise is imposed on the solution since the two-dimensional instabilities develop in the absence of perturbations. In three dimensions, the transverse velocity field u_2^+ is determined from continuity after the horizontal and vertical components are perturbed. The density field is not perturbed.

For all of the simulations, the kinematic viscosity is set to $\nu = 10^{-6}\,\mathrm{m^2\,s^{-1}}$, so that the wave Reynolds number is given by $Re_w = \omega_0/\nu k^2 = 2\,179$. In an effort to maintain the integrity of the interface up until breaking occurs, the scalar diffusivity κ is set to zero during wave growth while employing the background potential energy preserving scheme of (Fringer 2003). When the wave breaks at $t = t_b$ according to the criterion specified in § 4.1, we set κ so that the Prandtl number is $Pr = \nu/\kappa = 7$ and revert to the SHARP formulation of (Leonard 1987). Boundary conditions are periodic in the horizontal and free-slip on the upper and lower boundaries.

4. Initial instability

4.1. *Breaking criterion*

The total potential and kinetic energy within a volume V are defined as

$$E_p = \frac{g}{\rho_0}\int_V \rho z \,\mathrm{d}V, \tag{4.1}$$

$$E_k = \frac{1}{2}\int_V u_i u_i \,\mathrm{d}V. \tag{4.2}$$

While the maximum potential and kinetic energy for surface waves peaks before the critical breaking amplitude (Cokelet 1977), the kinetic and potential energy are monotonic before breaking for interfacial waves (Holyer 1979). When interfacial

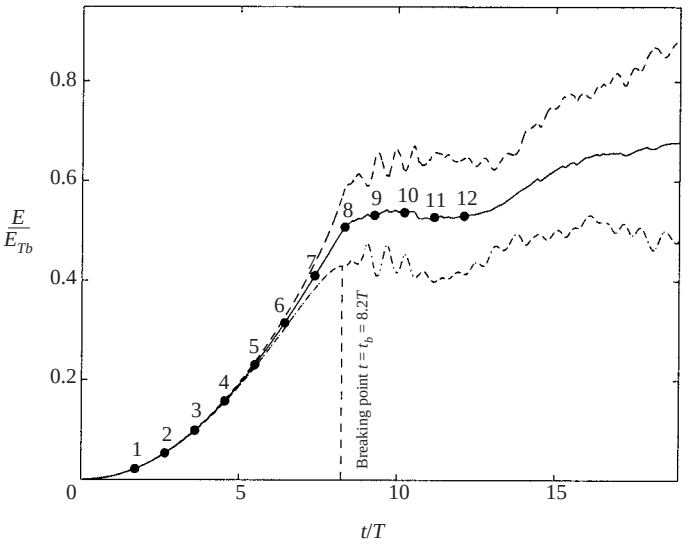

FIGURE 4. $-\cdot-$, potential and $--$, kinetic energy and —, half the total energy of a breaking interfacial wave with interface thickness $k\delta = \pi/10$, showing the breaking point t_b defined in equation (4.3). The filled circles and adjacent numbers correspond to the points in time in which contour plots are depicted in figure 5. Here E_{Tb} is the total energy at the point of breaking.

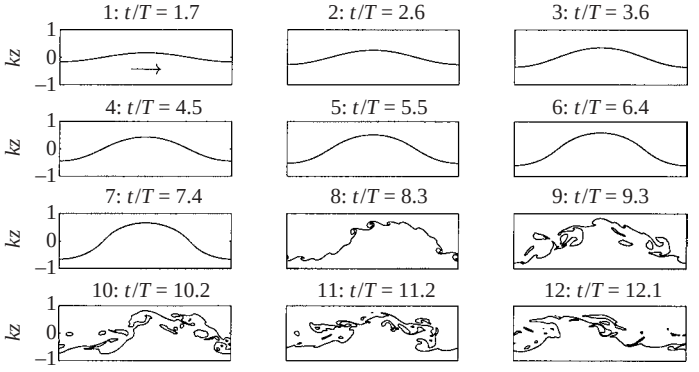

FIGURE 5. Contours of $\rho = 0$ for a two-dimensional breaking interfacial wave with interface thickness $k\delta = \pi/10$. The wave propagates from left to right, and each contour corresponds to a point in time depicted in figure 4.

waves break, the potential energy decreases as the wave overturns and fluid particles accelerate, causing an increase in the kinetic energy. Figure 4 depicts the kinetic and potential energy of a two-dimensional interfacial wave as it grows to its breaking amplitude while figure 5 depicts the corresponding contours of $\rho = 0$ at the particular points in time depicted in figure 4. From figure 5, the wave begins to break somewhere between points 7 and 9. This corresponds to the point in time in figure 4 in which the kinetic and potential energy begin to diverge sharply from one another because of breaking. Soon after the divergence, the kinetic energy grows while the potential energy decreases. This is indicative of a developing instability, and the point which is defined to be the incipient breaking time $t = t_b$. Therefore, breaking is defined as the

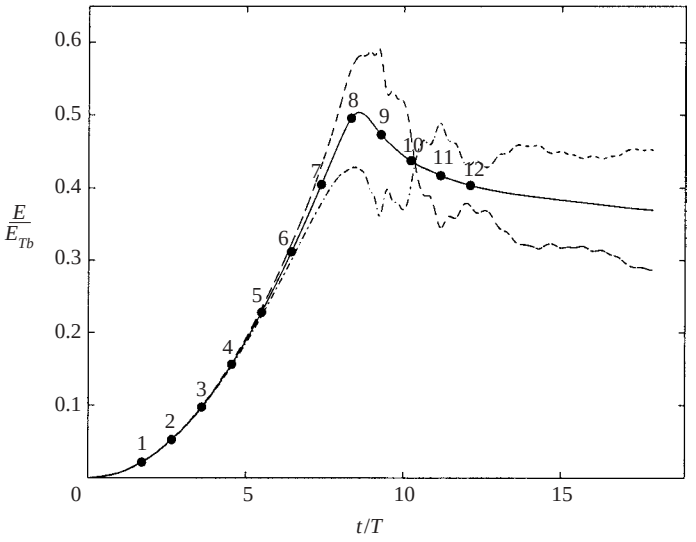

FIGURE 6. —·—, potential and – – –, kinetic energy and —, half the total energy of a breaking interfacial wave with interface thickness $k\delta = \pi/10$. The magnitude of the forcing function is ramped down over one period starting at $t/T = 7.7$. The filled circles and adjacent numbers correspond to the points in time in which contour plots are depicted in figure 7. Here E_{Tb} is the total energy at the point of breaking.

point at which the potential energy begins to drop, or the point at which

$$\left.\frac{\mathrm{d}E_p}{\mathrm{d}t}\right|_{t=t_b} = 0. \tag{4.3}$$

This occurs between points 7 and 8 at $t/T = 8.2$ in figure 4. The total energy continues to increase after $t = t_b$ because the forcing continues to add energy to the system.

In order to determine the breaking time t_b, two-dimensional simulations are performed with $f(t) = 1$ (corresponding to $t_f = \infty$) in equation (3.4). With t_b known, the breaking dynamics in the absence of forcing are then computed by applying the forcing function with $t_f = t_b - T/2$. At $t = t_f$, the magnitude of the forcing is gradually removed over one wave period T with the quarter-cosine function (3.4). Figures 6 and 7 depict the results of an interfacial wave in which the forcing is ramped down at $t = t_b - T/2$. Owing to the ramping down of the forcing magnitude, the unforced breaking simulations break slightly later in time than the forced simulations ($t_b = 8.2T$ forced *vs.* $t_b = 8.4T$ for the unforced). This is to be expected, since the instability grows faster for the forced simulation than for the unforced simulation. Nevertheless, the critical amplitude is not significantly affected.

4.2. *Critical breaking steepness*

We define the state of a stable interfacial wave in terms of the minimum Richardson number within the wave and the maximum Froude number within the wave. In terms of the wave steepness ka and interface thickness $k\delta$, the minimum Richardson number and maximum Froude number can be approximated with

$$Ri_{min} = \frac{N^2}{(\partial u/\partial z)^2} \approx \frac{1}{8}\frac{k\delta}{(ka)^2}, \tag{4.4}$$

$$Fr_{max} = \frac{u_{max}}{c} \approx ka, \tag{4.5}$$

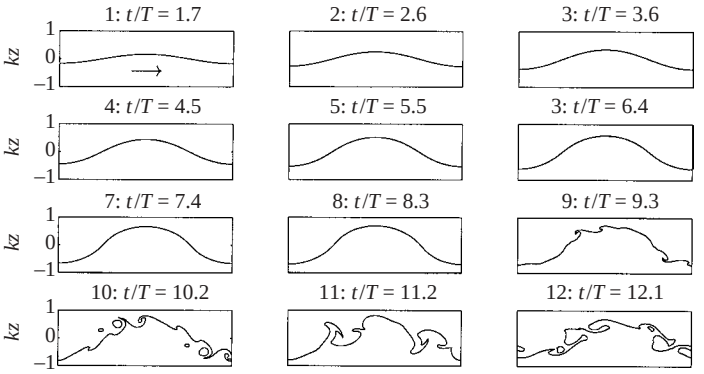

FIGURE 7. Contours of $\rho = 0$ for a two-dimensional breaking interfacial wave with interface thickness $k\delta = \pi/10$. The wave propagates from left to right, and each contour corresponds to a point in time depicted in figure 6. The magnitude of the forcing function is ramped down over one period starting at $t/T = 7.7$.

where we have approximated the maximum velocity to first order in ka as $u_{max} = a\omega_0$ and the shear and buoyancy frequency as

$$N^2 = -\frac{g}{\rho_0}\frac{\partial \rho}{\partial z} \approx \frac{2}{k\delta}\omega_0^2, \tag{4.6}$$

$$\frac{\partial u}{\partial z} \approx \frac{u(\zeta + \delta/4) - u(\zeta - \delta/4)}{\delta/2} = \frac{4u_{max}}{\delta} = 4\frac{ka}{k\delta}\omega_0. \tag{4.7}$$

This assumes that the maximum velocity occurs roughly at $z = \zeta \pm \delta/4$, where $z = \zeta$ is the mean interface line where $\rho = 0$. We define a maximum inverse Richardson number as

$$R_{max} = \frac{1}{4Ri_{min}}, \tag{4.8}$$

so that we have

$$R_{max} = \frac{2\alpha_{Ri}(ka)^2}{k\delta}, \tag{4.9}$$

where α_{Ri} is a function of $k\delta$ and is computed in order to account for highly nonlinear effects when ka and $k\delta$ become large. The state of an interfacial wave then follows the trajectory in the (R_{max}, Fr_{max})-plane that is defined by

$$R_{max} = \frac{2\alpha_{Ri}Fr_{max}^2}{k\delta}. \tag{4.10}$$

We compute the value of α_{Ri} for each $k\delta$ by generating stable interfacial waves with increasing steepness and computing α_{Ri} that satisfies a least-squares fit to the computed (R_{max}, Fr_{max})-trajectory of that interfacial wave, where the Richardson number and Froude number are computed directly from the simulation results. The Richardson number is computed readily from the simulation results since the vertical density and velocity gradients can be computed numerically. However, in order to compute the Froude number, an estimation of the phase speed of the wave is required. The phase speed is determined by computing a phase speed c that minimizes the time rate of change of the density field in a reference frame moving with the wave. In a frame moving with the wave, the streamlines are parallel to the lines of constant density, and in the absence of scalar diffusivity, there is no change in the density field.

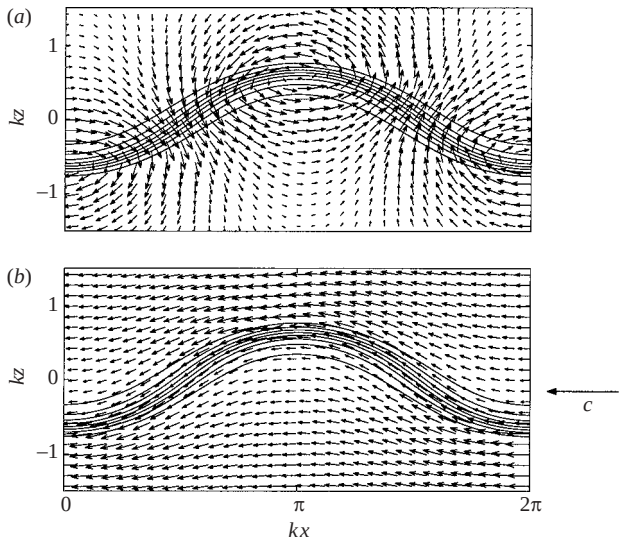

FIGURE 8. Velocity and density fields of a right-propagating interfacial wave in (*a*) a stationary reference frame, and (*b*) a frame that moves with the wave to the right at speed c. The interface thickness is $k\delta = 2\pi/5$, the steepness is $ka = 0.61$, and the wave speed is $c/c_0 = 0.95$.

A global measure of the time rate of change of the density field in a frame moving at the wave speed c is given by the 2-norm

$$E_2^2(c) = \int_V \left(\frac{\partial \rho}{\partial t}\right)^2 \mathrm{d}V = \int_V \left[(u-c)\frac{\partial \rho}{\partial x} + w\frac{\partial \rho}{\partial z}\right]^2 \mathrm{d}V, \tag{4.11}$$

where V represents the volume of the computational domain. Differentiating with respect to c results in the phase speed that minimizes $E_2(c)$,

$$c = \frac{\displaystyle\int_V (u\rho_x + w\rho_z)\,\rho_x \,\mathrm{d}V}{\displaystyle\int_V \rho_x^2 \,\mathrm{d}V}. \tag{4.12}$$

This minimization problem effectively computes a phase speed c that minimizes the velocity components normal to the lines of constant density, and hence aligns the streamlines with the constant density lines. Figures 8(*a*) and 8(*b*) depict the velocity field of an interfacial wave in a stationary frame and one moving at the wave speed c.

Figure 9 depicts trajectories of stable waves with increasing $k\delta$. Each point in the trajectories in figure 9 corresponds to the location of a steady-state interfacial wave after the forcing is removed. Because viscosity and transient effects cause the steady-state location of the interfacial waves to deviate slightly from their initial locations, the points in figure 9 correspond to average locations in the (R_{max}, Fr_{max})-plane. These results show that the nonlinear correction factor is given by

$$\alpha_{Ri} = 1.3(k\delta)^{1/2}, \tag{4.13}$$

which indicates that a better approximation for the trajectories in the (R_{max}, Fr_{max})-plane, at least for the $k\delta$ in the range covered in this paper, is given by

$$R_{max} = \frac{2.6 Fr_{max}^2}{(k\delta)^{1/2}}. \tag{4.14}$$

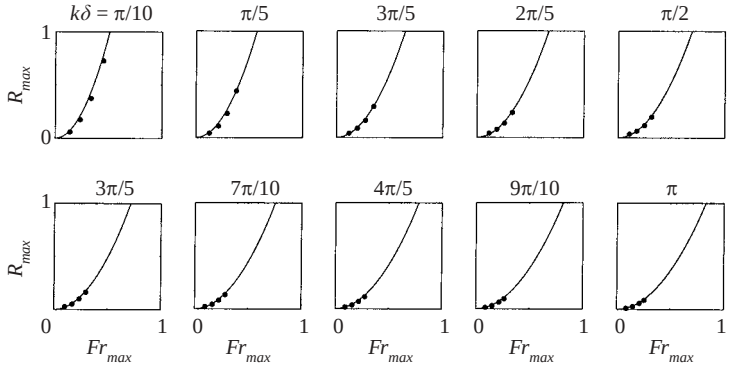

FIGURE 9. Trajectories of stable interfacial waves with increasing $k\delta$ in the (R_{max}, Fr_{max})-plane. The points indicate the mean locations of the stable waves in the plane after release of forcing, and the solid lines depict the best fit of equation (4.10) by adjusting α_{Ri}.

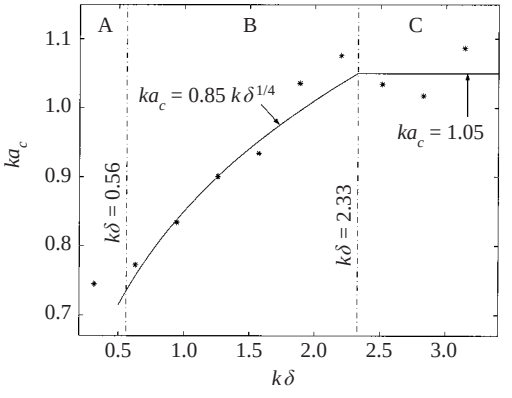

FIGURE 10. Critical breaking steepness as a function of the interface thickness $k\delta$. The data points ($\star$) depict the critical steepness for each $k\delta$ computed with the criterion in § 4.1, while the solid line depicts the theoretical critical steepness lines obtained from a least-squares fit to the data. The vertical lines separate the three regimes (A, B, C) discussed in the text.

This approximation does not result from an asymptotic expansion in powers of ka and $k\delta$, but rather, holds for the ka and $k\delta$ covered in this paper, that is, $0 \leqslant ka \leqslant 1$ and $\pi/10 \leqslant k\delta \leqslant \pi$. Asymptotic expansions in powers of $k\delta$ such as those performed by Phillips (1977) and Jou & Weissman (1987) are not valid for such large values.

We can use the equation for the trajectories in the (R_{max}, Fr_{max})-plane to determine the instability that governs the critical steepness ka of an interfacial wave with interface thickness $k\delta$. From linear stability theory (Drazin 1977), a shear instability results when $R_{max} > 1$, but this condition is not valid for the highly nonlinear and unsteady waves studied here. However, we can conclude that waves that break along lines of constant R_{max} break because of a shear instability, albeit a highly modified shear instability, while waves that break at a constant Fr_{max} break bacause of a convective instability. We will refer mostly to the state of waves in terms of $k\delta$ and ka, but this translates directly to a point in the (R_{max}, Fr_{max})-plane.

Figure 10 depicts the critical breaking steepness ka_c as a function of the interface thickness $k\delta$. The data points ($\star$) represent critical breaking steepnesses computed with the criterion developed in § 4.1 for ten different interfacial waves with interface

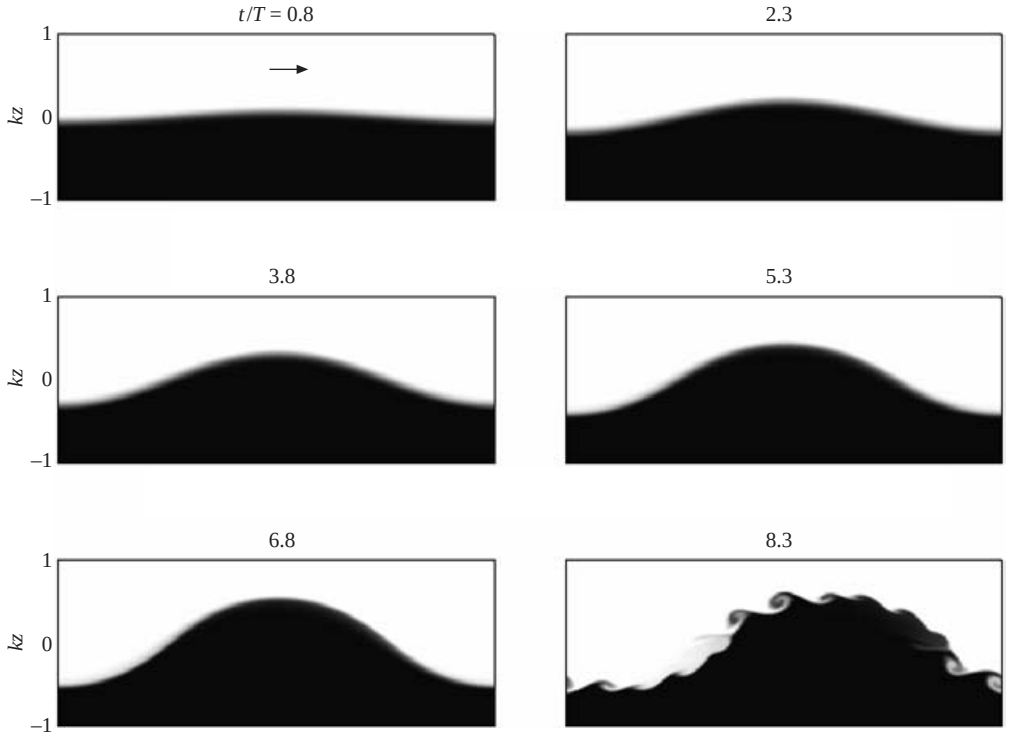

FIGURE 11. Evolution of a two-dimensional breaking interfacial wave with non-dimensional interface thickness $k\delta = \pi/10$ that breaks in regime A in figure 10. The wave propagates from left to right.

thickness in the range $\pi/10 \leqslant k\delta < \pi$ forced until breaking. The scatter results from the transient oscillations in the steepness that cause E_p to be slighly out of phase with ka, and hence leads to slight discrepancies in the point at which $\mathrm{d}E_p/\mathrm{d}t = 0$. The solid line depicts the theoretical critical steepness limit derived from a least-squares fit to the data. The results show that the particular instability that limits the steepness of a breaking interfacial wave can be divided into the three regimes shown, namely A: $k\delta < 0.56$, B: $0.56 \leqslant k\delta < 2.33$ and C: $k\delta \geqslant 2.33$.

Figure 11 depicts growth to instability of an interfacial wave in regime A. The dynamics of waves in this regime is covered by (Troy 2003), who provides the following argument. The critical steepness is limited by a Kelvin–Helmholtz shear instability at the interface. Clockwise Kelvin–Helmholtz billows form in the trough where the vertical shear is positive, while counterclockwise Kelvin–Helmholtz billows form at the crest where the vertical shear is negative. For waves in regime A, the wavelength of the most rapidly growing disturbance arising from the shear instability is less than 1/4 of the wavelength of the interfacial wave. If the wavelength of the most rapidly growing disturbance of a shear instability is given by $\lambda_{KH} = 2.8\delta$ (Hazel 1972), and these disturbances grow uninhibited within interfacial waves with wavelengths of at least $4\lambda_{KH}$, then this corresponds to interfacial waves with $k\delta < 0.56$. Effectively, the shear instability 'fits' into the interfacial waves in regime A.

When the interface thickness increases beyond $k\delta = 0.56$, the dominant instability is also a shear instability, since the critical steepness of these waves closely follows the line for which $ka_c = 0.85k\delta^{1/4}$. This corresponds to a line of constant $R_{max} = 1.85$ in the

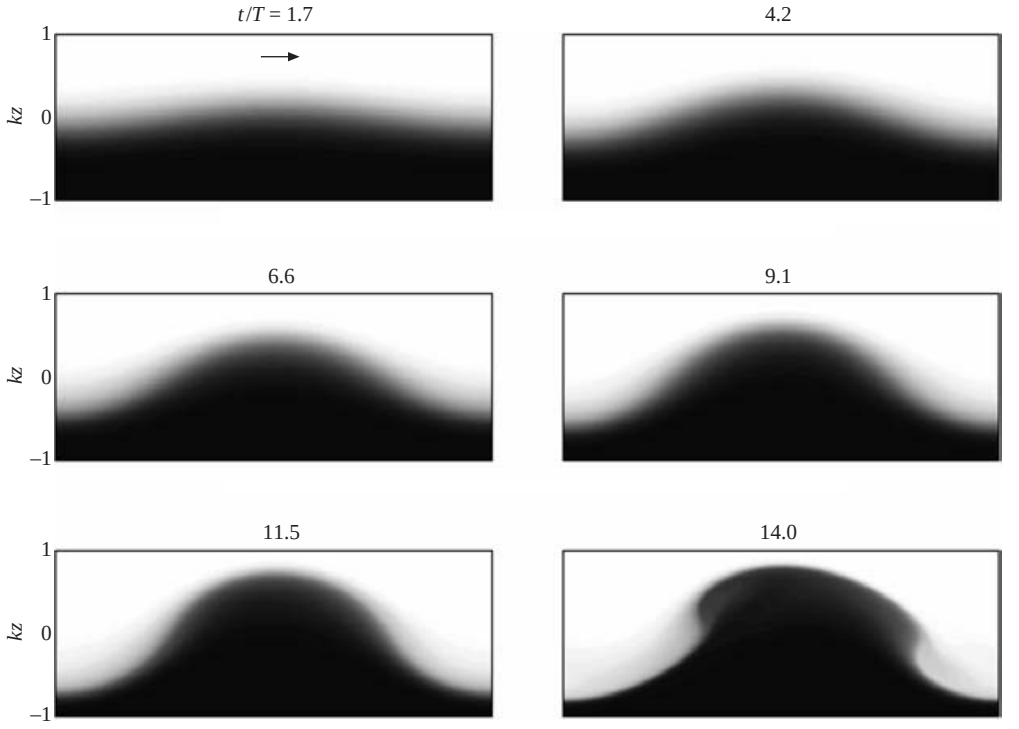

FIGURE 12. Evolution of a two-dimensional breaking interfacial wave with non-dimensional interface thickness $k\delta = \pi/2$ that breaks in regime B in figure 10. The wave propagates from left to right.

(R_{max}, Fr_{max})-plane, or a line of constant minimum Richardson number of $Ri_{min} = 0.13$. Interfacial waves therefore do not necessarily break at the critical Richardson number for linear stability of $Ri_{min} = 0.25$. In this regime, the size of the Kelvin–Helmholtz billows is of the same order of magnitude as the amplitude of the interfacial wave, as shown in figure 12. As a result, the wave appears to overturn owing to a convective instability when a statically unstable situation occurs at $t/T = 14.0$. At this point, the phase speed of the wave has decreased and indeed the maximum Froude number of the wave, $Fr_{max} = u_{max}/c$, does exceed unity. However, the initial instability is still brought about by a shear instability that effectively increases the maximum velocity and reduces the wave speed so that the Froude number becomes supercritical. This property is what defines the waves in regime B: the capability of the Kelvin–Helmholtz billows to induce a two-dimensional convective instability. The size of the Kelvin–Helmholtz billows in the interfacial waves in regime A are not large enough to induce such a situation, and hence Fr_{max} does not exceed unity for these waves.

The interface thickness of the waves in regime C is so large that the Kelvin–Helmholtz billows cannot form and hence the instability is purely convective. These waves are limited to a maximum steepness of roughly $ka_c = 1.05$, as shown in figure 10, which shows that the approximation $Fr_{max} = ka$ holds very well even for such highly nonlinear waves. This is consistent with the findings of (Holyer 1979), who shows that Boussinesq irrotational waves are limited to a steepness of $ka_c = 1.1$, indicating that interfacial waves with thick interfaces behave as irrotational waves because the shear at the interface is negligible. Instead, nonlinear forces within the wave cause the maximum fluid velocity within the wave to exceed the wave speed before a

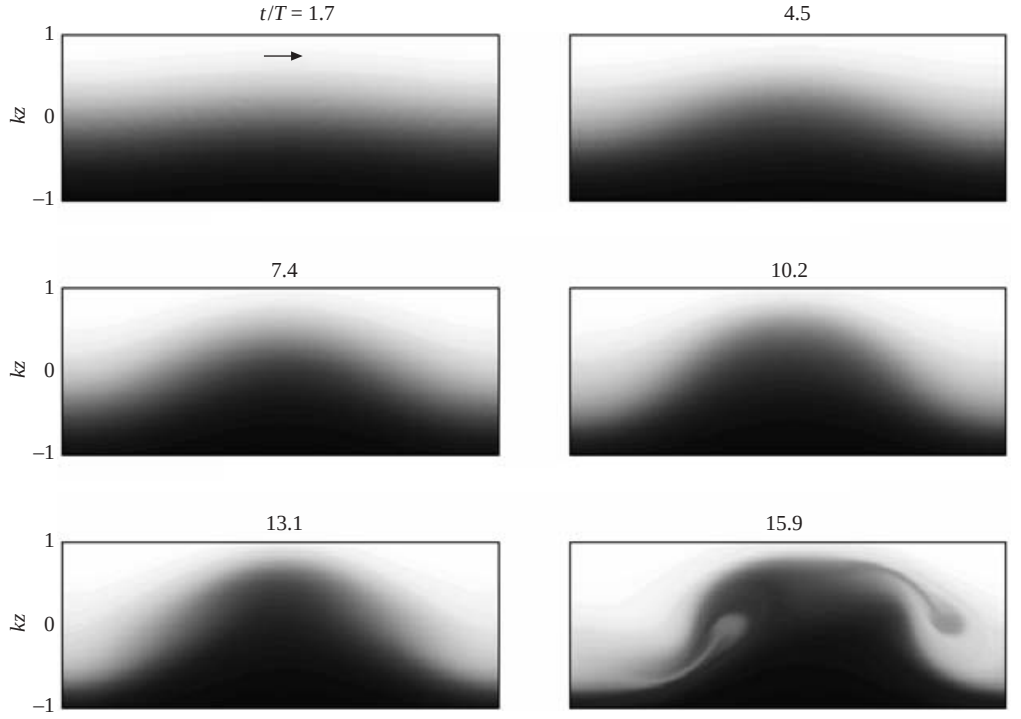

FIGURE 13. Evolution of a two-dimensional breaking interfacial wave with non-dimensional interface thickness $k\delta = \pi$ that breaks in regime C in figure 10. The wave propagates from left to right.

Kelvin–Helmholtz instability can develop, as shown in figure 13. The lack of shear-induced billows leads to less spectacular two-dimensional breaking for the waves in regime C. Statically unstable regions of fluid move out ahead of the wave crest where the local Froude number becomes supercritical, leading to more localized regions of instability. This was shown to be the case for the waves in the experiments of Thorpe (1978).

To summarize, the initial instability of breaking interfacial waves is due to shear when the interface thickness is less than $k\delta = 2.33$. When $k\delta < 0.56$, the length scale of the Kelvin–Helmholtz billows is smaller than one quarter of the wavelength of the interfacial wave, and hence they grow less impeded by the wave and do not induce a convective instability (Troy 2003). Larger interface thickness waves develop more energetic Kelvin–Helmholtz billows that lead to a convective instability because the billows reduce the phase speed of the wave so that $Fr_{max} > 1$. When the interface thickness is too large, Kelvin–Helmholtz billows do not form and the instability is purely convective and much weaker. The relative size of the billows plays an important role in the mixing and dissipation that results in the three-dimensional dynamics that ensue after the initial two-dimensional instabilities. This is discussed in § 5.

5. Three-dimensional dynamics and mixing

5.1. *Description of breaking dynamics*

Figures 14, 15 and 16 depict the isosurface of $\rho = 0$ for breaking interfacial waves in the three regimes depicted in figure 10. All three figures show how three-dimensionality

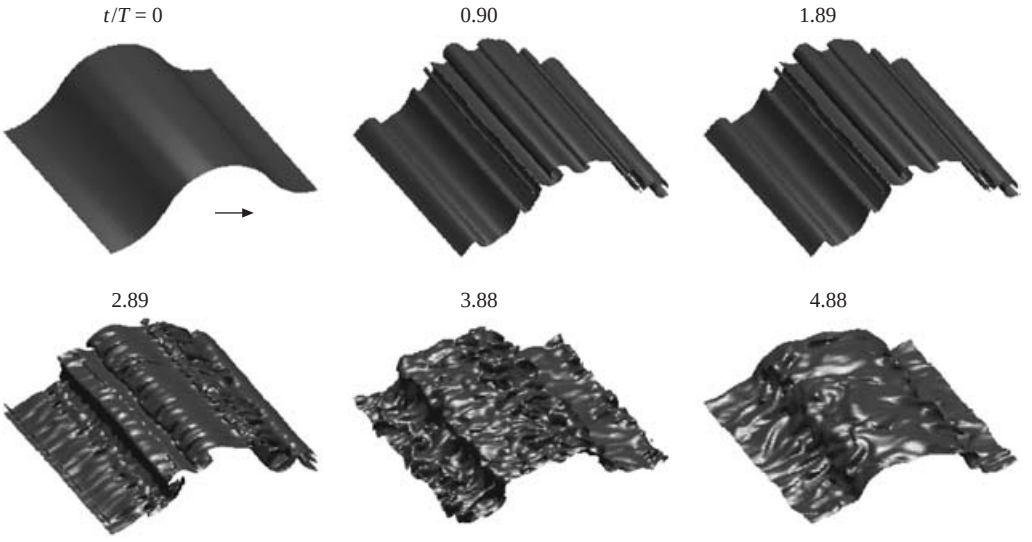

FIGURE 14. Isosurfaces of $\rho = 0$ for a breaking interfacial wave with $k\delta = \pi/10$, corresponding to regime A in figure 10, at 6 points in time after release of forcing. The wave propagates from left to right.

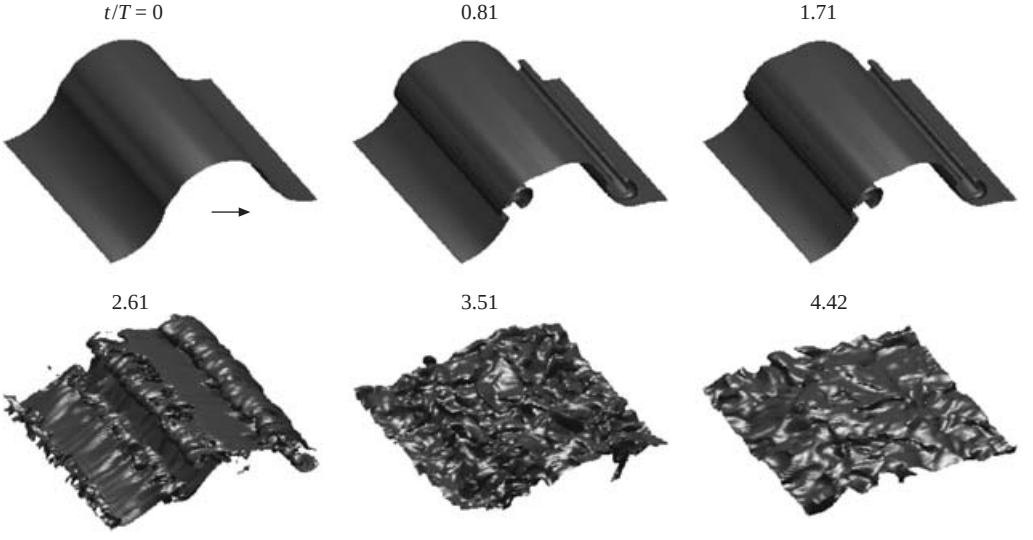

FIGURE 15. Isosurfaces of $\rho = 0$ for a breaking interfacial wave with $k\delta = \pi/2$, corresponding to regime B in figure 10, at 6 points in time after release of forcing. The wave propagates from left to right.

is not evident until after the cross-stream rolls develop as a result of an initial two-dimensional instability. The waves in figures 14 and 15, corresponding to regimes A and B in figure 10, generate regions which are susceptible to a cross-stream convective instability only after development of the initial two-dimensional shear instability. Likewise, the wave in figure 16, corresponding to regime C in figure 10, develops three-dimensionality after the initial two-dimensional convective instability. Because the time scale associated with the shear instability is shortest for the wave with the thinnest interface, the wave in figure 14 develops the Kelvin–Helmholtz

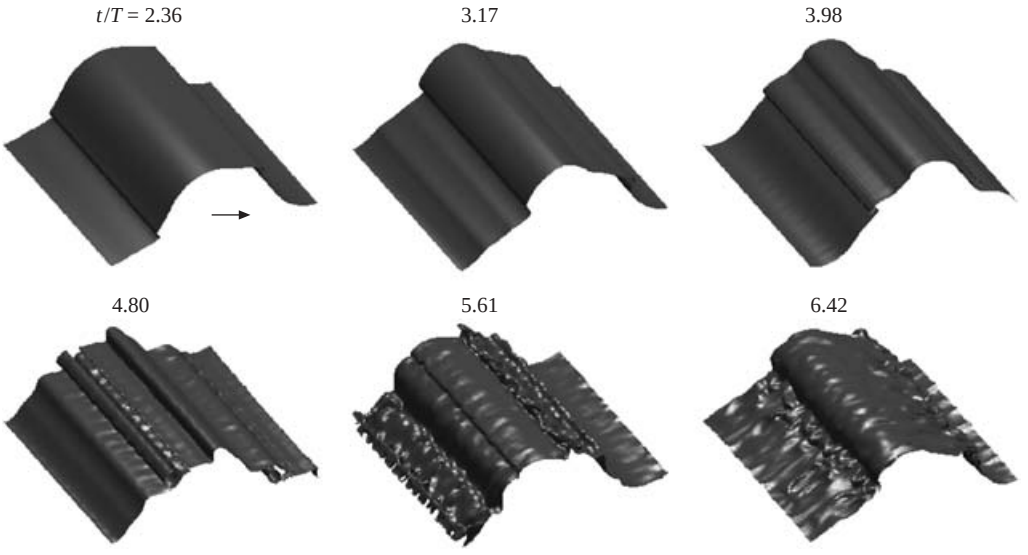

FIGURE 16. Isosurfaces of $\rho = 0$ for a breaking interfacial wave with $k\delta = \pi$, corresponding to regime C in figure 10, at 6 points in time after release of forcing. The wave propagates from left to right.

billows sooner than those in figure 15. The three-dimensional instabilities develop the latest for the wave in regime C, indicating that the weakest instability is the initial convective two-dimensional instability for large $k\delta$. Clearly, the wave that loses the most energy of the three is that in regime B. By the sixth frame, very little of the initial wave profile is left over, while a clear wave signature is left over for the waves in regimes A and C. This is discussed in more detail in § 5.2.

Unlike critical layers, the breaking mechanism for interfacial waves is unambiguous. First, depending on the regime, either Kelvin–Helmholtz billows or Rayleigh–Taylor billows develop at the crest and troughs of the waves. Then, energy is transferred to the cross-stream dimension through convective instabilities that develop as a result of the initial two-dimensional billows. These cross-stream convective instabilities develop in regions where the fluid is in a statically unstable situation for enough time for the convectively driven three-dimensional flow to manifest itself. Therefore, because this statically unstable situation can only arise from the development of the two-dimensional billows, the three-dimensional convective instability is limited to occurring after the initial two-dimensional billows form. Just as Winters & D'Asaro (1994) found for critical layers, the cross-stream instability for interfacial waves is dominated by a convective instability which generates longitudinal rolls that account for most of the wave breaking and energy loss. These longitudinal rolls are reported by Dörnbrack (1998) to account for a significant portion of the energy loss and mixing in critical layers as well.

Figures 17, 18 and 19 depict isosurfaces of $\rho = 0$ and longitudinal vorticity ($\omega_1 = u_{3,2} - u_{2,3}$) for interfacial waves in regimes A, B and C in figure 10, respectively. The vorticity isosurfaces represent the longitudinal vorticity with frequency $\omega_1 = \omega/2$, and are shown at a point in time when the cross-stream kinetic energy is maximized for each case. This longitudinal vorticity grows initially as a result of a statically unstable situation that results from the initial two-dimensional instability. In figures 20(a) and 20(b), the contours of longitudinal vorticity exist only in the statically unstable regions

FIGURE 17. Isosurfaces of $\rho = 0$ (red) and longitudinal vorticity ω_1 for a breaking interfacial wave with interface thickness $k\delta = \pi/10$, corresponding to regime A in figure 10, when the cross-stream kinetic energy is maximized at $t/T = 2.33$ after release of forcing. Blue and green isosurfaces represent positive and negative longitudinal vorticity of magnitude $\omega_1/\omega = 1/2$. The wave propagates from left to right.

formed by the two-dimensional Kelvin–Helmholtz billows, while in figure 20(*c*), longitudinal vorticity exists in statically unstable regions formed by the two-dimensional Rayleigh–Taylor instability. The longitudinal vorticity that forms for all three cases is further enhanced by the stretching of vortex filaments by the two-dimensional billows. The relative strength of the longitudinal vorticity, and therefore the length scale of the longitudinal rolls, is set by the local thickness of the statically unstable region that develops from the two-dimensional instability. Because the time scale of the formation of the convective billows is inversely proportional to the local thickness of the statically unstable region, longitudinal vorticity grows only when the local thickness becomes small enough such that the time scale of the instability drops below the overturning time scale of the overlying two-dimensional instability that feeds energy into the longitudinal rolls. Therefore, because the time scale of the overlying two-dimensional instability grows with increasing $k\delta$, so does the length scale of the longitudinal rolls, albeit substantially smaller than $k\delta$. As discussed in the next section, it is the length scale of the overlying two-dimensional instability that governs the mixing and dissipation of the breaking process.

5.2. *Irreversible energy changes and the mixing efficiency*

According to Winters *et al.* (1995), the potential energy can be split into its available and background components so that

$$E_p = E_b + E_a. \tag{5.1}$$

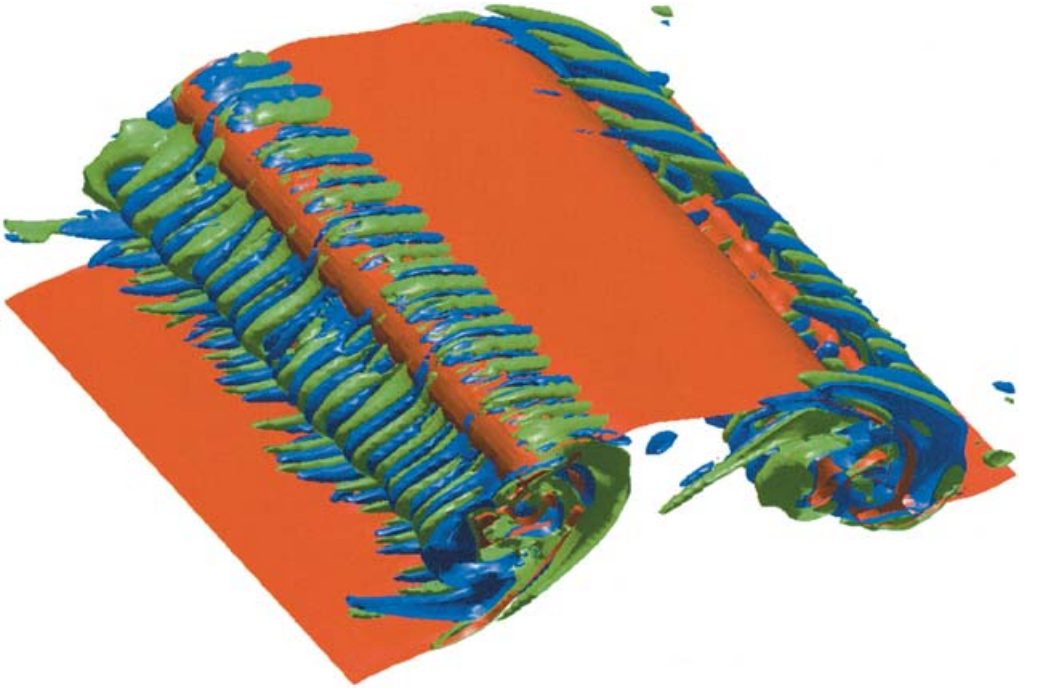

FIGURE 18. Isosurfaces of $\rho = 0$ (red) and longitudinal vorticity ω_1 for a breaking interfacial wave with interface thickness $k\delta = \pi/2$, corresponding to regime B in figure 10, when the cross-stream kinetic energy is maximized at $t/T = 2.93$ after release of forcing. Blue and green isosurfaces represent positive and negative longitudinal vorticity of magnitude $\omega_1/\omega = 1/2$. The wave propagates from left to right.

The background potential energy, E_b, represents the potential energy of the system if it were allowed to come to rest adiabatically. That is, if at some instant in time the scalar diffusivity vanished, then eventually the flow would come to rest in some statically stable state in which the potential energy was equal to the background potential energy. A general definition of the background potential energy is given by (Winters *et al.* 1995),

$$E_b = \frac{g}{\rho_0} \int_V \rho(z^*) z^* \, \mathrm{d}V, \tag{5.2}$$

and it evolves according to

$$\frac{\mathrm{d}E_b}{\mathrm{d}t} = \phi_d = \frac{g\kappa}{\rho_0} \int_V z^* \nabla^2 \rho(z^*) \, \mathrm{d}V, \tag{5.3}$$

where $\rho(z^*)$ is the density distribution in its background state. Computation of the background potential energy is expensive (Fringer 2003) because it requires a sorting of the density field in ascending order. We employ the Quicksort algorithm (Roberts 1998), which requires $O(N \log N)$ operations to sort an array of length N. Since the three-dimensional computations we perform have $N = 128^3$ finite volumes, a slower algorithm would be unaccepatable. After a direct computation of the background potential energy is made, the available potential energy can be obtained with $E_a = E_p - E_b$. The potential energy is in turn related to the total energy E_T and kinetic energy

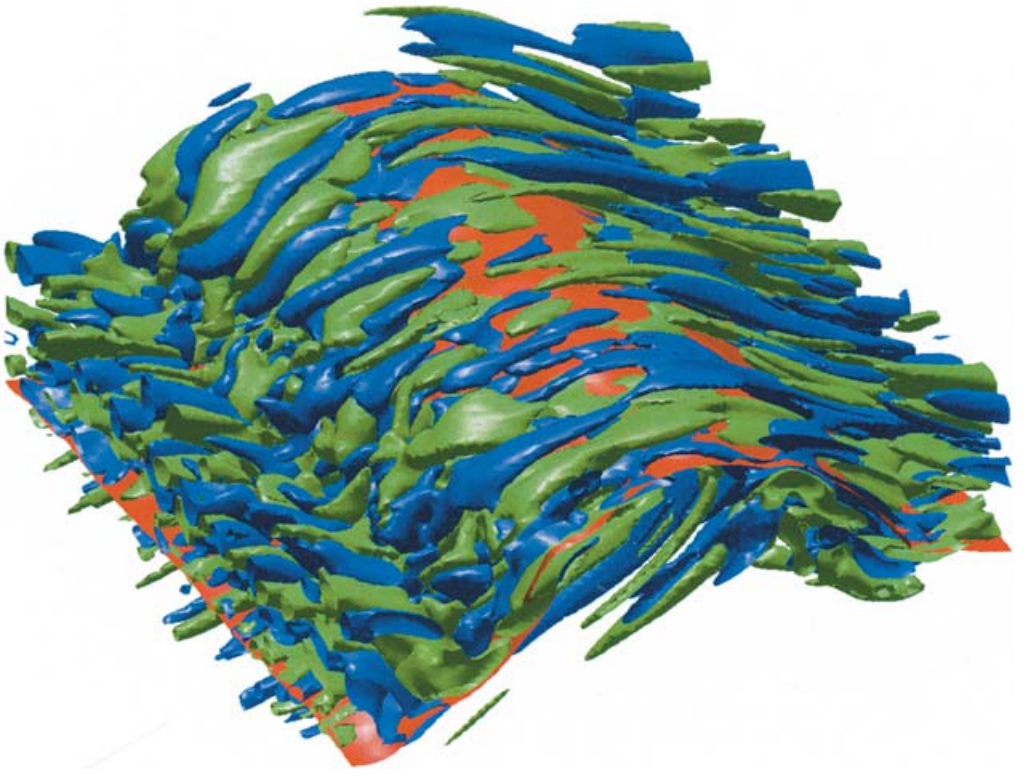

FIGURE 19. Isosurfaces of $\rho = 0$ (red) and longitudinal vorticity ω_1 for a breaking interfacial wave with interface thickness $k\delta = \pi$, corresponding to regime C in figure 10, when the cross-stream kinetic energy is maximized at $t/T = 3.66$ after release of forcing. Blue and green isosurfaces represent positive and negative longitudinal vorticity of magnitude $\omega_1/\omega = 1/2$. The wave propagates from left to right.

E_k via

$$\frac{\mathrm{d}E_k}{\mathrm{d}t} + \frac{\mathrm{d}E_p}{\mathrm{d}t} = -\epsilon, \tag{5.4}$$

where the volume integrated dissipation is given by

$$\epsilon = \nu \int_V \frac{\partial u_i}{\partial x_j} \frac{\partial u_i}{\partial x_j} \mathrm{d}V. \tag{5.5}$$

Figures 21(*a*) and (*b*) depict the energy budgets of breaking interfacial waves with $k\delta = \pi/10$ (*a*) and $k\delta = \pi/2$ (*b*) as departures from their values just before breaking at $t = t_b$ and normalized by the maximum available potential energy, $E_{a,max}$, which is the available potential energy at $t = t_b$. Upon breaking for both cases, there is an immediate rise in the kinetic energy at the expense of the available potential energy. The rise in the kinetic energy results from the creation of the longitudinal rolls that result from the cross-stream convective instability. Soon after, the kinetic energy drops along with the available potential energy until the available potential energy asymptotes to a lower level, at which a lower-amplitude wave exists with a thicker interface, as shown in figures 22 and 23. These figures depict the wave-averaged density profiles of the waves just before and 10 periods after breaking, where the

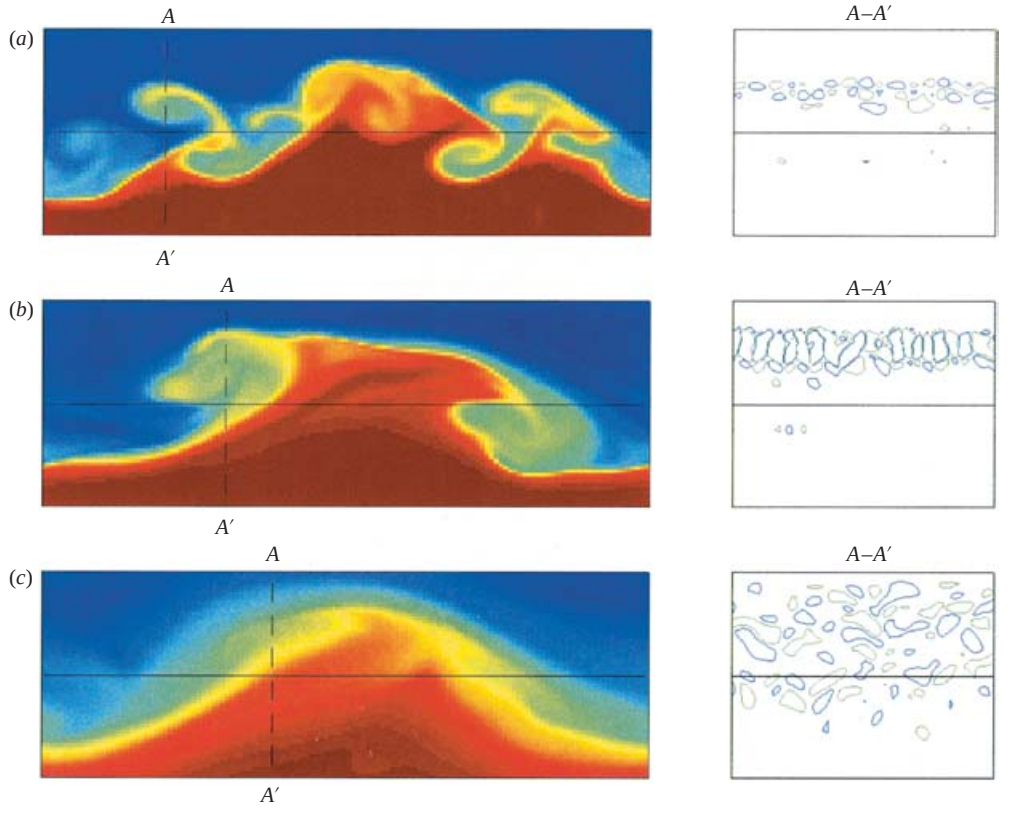

FIGURE 20. Surface plots of the wave-averaged density field and the associated contours of positive (blue) and negative (green) longitudinal vorticity of magnitude $\omega_1/\omega = 1/2$ in plane $A - A'$ when the cross-stream kinetic energy is maximized. The interface thickness and time are given by (*a*) $k\delta = \pi/10$, $t/T = 2.33$; (*b*) $k\delta = \pi/2$, $t/T = 2.93$; (*c*) $k\delta = \pi$, $t/T = 3.66$. The wave propagates from left to right.

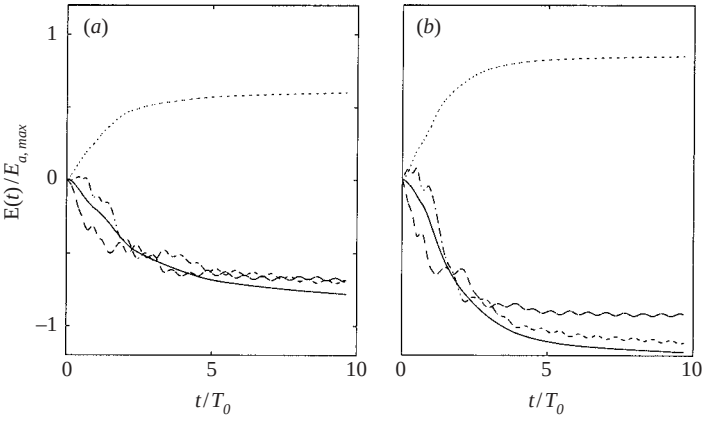

FIGURE 21. Energy budgets of breaking interfacial waves with interface thickness (*a*) $k\delta = \pi/10$ and (*b*) $k\delta = \pi/2$, normalized by the maximum available potential energy. The time is relative to t_b, the point at which breaking occurs. Legend: —, E_T; – – –, E_a; —·—, E_k; · · ·, E_b.

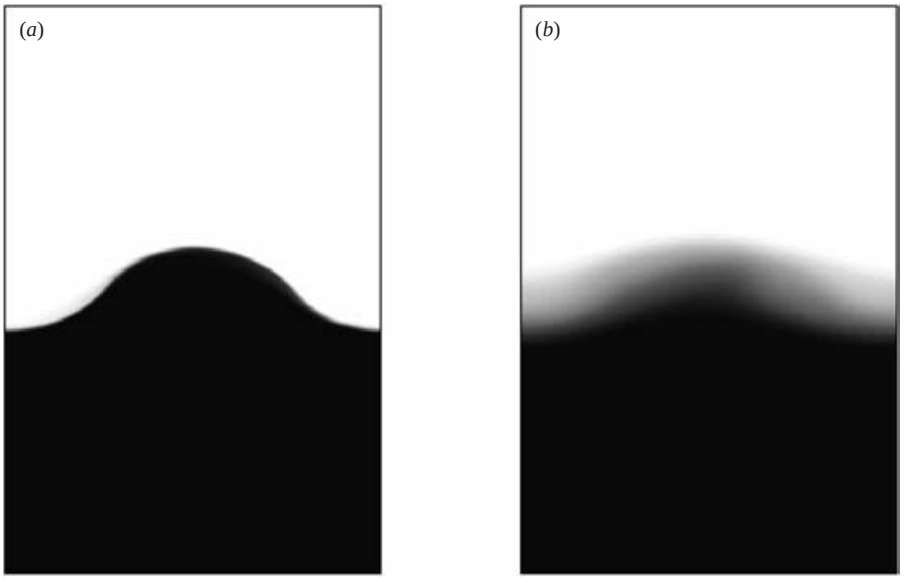

FIGURE 22. Surface plots of the wave-averaged density field from equation (5.6) of an interfacial wave with an initial interface thickness of $k\delta = \pi/10$ (*a*) before and (*b*) 10 periods after breaking.

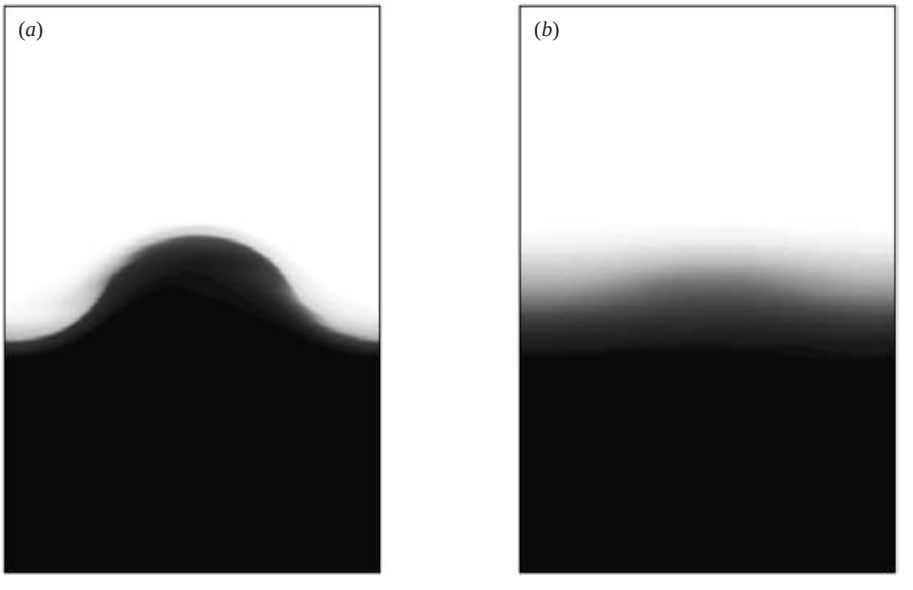

FIGURE 23. Surface plots of the wave-averaged density field from equation (5.6) of an interfacial wave with an initial interface thickness of $k\delta = \pi/2$ (*a*) before and (*b*) 10 periods after breaking.

wave-averaged density field $\overline{\rho}$ is given by

$$\overline{\rho}(x, z, t) = \frac{1}{W} \int_0^W \rho(x, y, z, t)\, \mathrm{d}y, \tag{5.6}$$

and W is the width of the domain. The wave-averaged density fields show how the

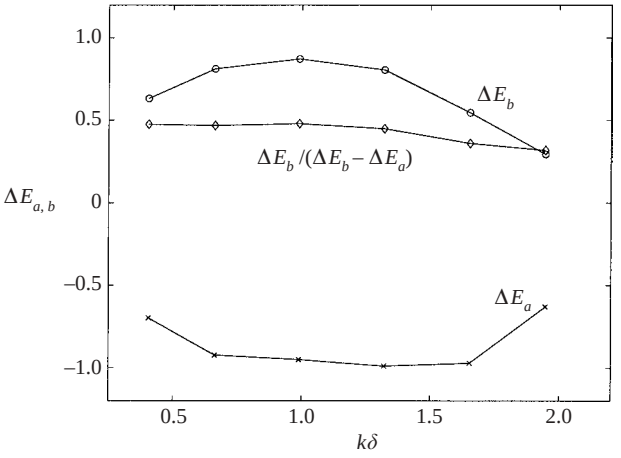

FIGURE 24. Change in the available and background potential energy and the bulk mixing efficiency, $\eta_B = \Delta E_b/(\Delta E_b - \Delta E_a)$, during wave breaking as a function of the interface thickness at the onset of breaking.

effect of the breaking process is to lose a significant portion of the wave amplitude and to increase the interface thickness. The increased interface thickness for both cases results in the increase in the background potential energy in figures 21(*a*) and 21(*b*). Because interfacial diffusion accelerates immediately upon wave breaking owing to the ensuing turbulence, the background potential energy rises monotonically until it asymptotes to the background potential energy of a wave with a thicker interface.

Figure 24 depicts the change in available and background potential energy resulting from wave breaking as a function of the mean interface thickness at the onset of breaking (in general, this is slightly different from the initial interface thickness of the interface at the onset of forcing). The figure also depicts the ratio of the total gain in the background potential energy to the sum of the loss of available potential energy and the gain in the potential energy. This is a measure of how efficiently the background potential energy rises at the expense of the available potential energy of the wave. Michallet & Ivey (1999) define the mixing efficiency in a similar manner for their experiments of breaking interfacial waves on a sloping boundary. Following their work, we define the bulk mixing efficiency as

$$\eta_B = \frac{\Delta E_b}{\Delta E_b - \Delta E_a}, \tag{5.7}$$

where ΔE_a and ΔE_b are the total change in the available and background potential energy resulting from wave breaking. Both arise from irreversible changes in energy. The available potential energy is lost to the kinetic energy of the flow, which in turn loses its energy to dissipation. The background potential energy rises irreversibly with interfacial diffusion which is accelerated by the breaking process. Clearly, there is a maximum loss of available potential energy and a maximum gain in background potential energy roughly at $k\delta = 1$, which corresponds to a wave in regime B in figure 10. This is the point at which energy is transferred most efficiently into the longitudinal rolls that account for most of the mixing and dissipation in the wave. The length scale of the longitudinal rolls as well as the cross-stream Kelvin–Helmholtz

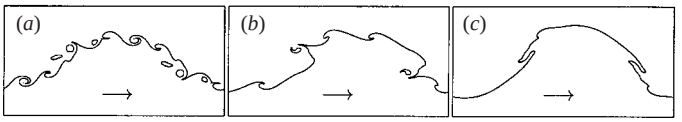

FIGURE 25. Contours of $\rho = 0$ for waves with three different interface thicknesses during breaking. Dissipation and mixing are maximized when $k\delta \sim ka$. The waves propagate from left to right.

billows is set by the interface thickness. How much available potential energy is lost by the wave is set by the ratio of the interface thickness to the steepness. If the interface is very thin, then the Kelvin–Helmholtz billows are not energetic enough to influence the overall character of the wave, and hence mixing and dissipation are limited by eddies that are of the order of $k\delta$, as shown in figure 25(*a*). However, if the interface thickness is of the order of the amplitude such that $k\delta \sim ka$, then the size of the eddies induced by the Kelvin–Helmholtz instability is roughly equal to the amplitude of the wave. This results in wave overturning in its most catastrophic sense, and hence results in a maximum energy transfer to the longitudinal rolls which results in the most dissipation and scalar mixing, as shown in figure 25(*b*). Too thick an interface results in two-dimensional convective billows which are too weak to significantly affect the overall character of the wave, as shown in figure 25(*c*). In addition to the size of the billows for the thicker interface, the strength of the Kelvin–Helmholtz instability weakens as well with increased interface thickness, up until the point at which the Kelvin–Helmholtz billows vanish and the initial instability is dominated by weak two-dimensional convective instabilities, as was shown in § 4.2. This weak character of the initial two-dimensional instability in turn weakens the associated mixing and dissipation during wave breaking. However, because a decrease in the available potential energy is counteracted by an increase in the background potential energy, the bulk mixing efficiency is a weak function of the interface thickness, and the average value is $\eta_B = 0.42 \pm 0.07$.

To obtain a better understanding of the mixing and dissipation of the breaking process, it is useful to analyse the instantaneous rate of change of the background potential energy ϕ_d from equation (5.3) as well as the dissipation ϵ from equation (5.5). Figure 26 depicts the non-dimensional rates $\phi_d^* = \phi_d/(\omega_0 E_{a,max})$ and $\epsilon^* = \epsilon/(\omega_0 E_{a,max})$ for four different interface thicknesses. The irreversible energy exchanges reach peak values soon after breaking. As previously discussed, the largest peaks in the dissipation and mixing occur for $k\delta$ in the intermediate ranges. Multiple peaks in the dissipation and mixing curves for the thinner interfaces occur as a result of secondary and possible tertiary breaking owing to pairing of Kelvin–Helmholtz induced cross-stream vortices. Each pairing event transfers wave energy into longitudinal convective rolls which further enhance dissipation and mixing. For large interface thicknesses, the initial two-dimensional convective rolls do not induce vortex pairing, but rather, transfer energy into alternate wave components which interact in a nonlinear manner and generate much weaker convective patches. While thicker waves do not dissipate as much wave energy during the initial breaking event, the remaining wave energy acts to enhance further intermittent and localized smaller-scale breaking events through the nonlinear interaction of these multiple wavenumbers. These events occur over periods that extend beyond the time period shown in figure 26.

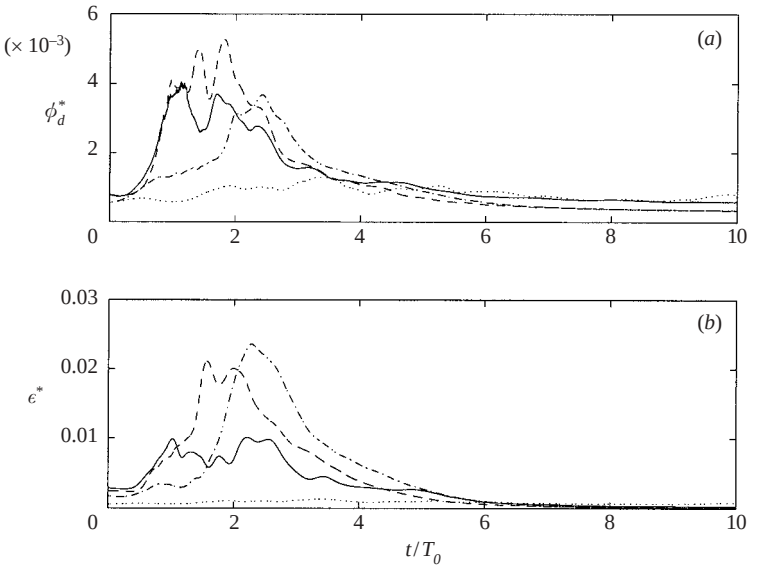

FIGURE 26. Non-dimensional instantaneous rates of energy exchange ϕ_d^* and ϵ^* for four different interface thicknesses. —, $k\delta = \pi/10$; – – –, $k\delta = 3\pi/10$; —·—, $k\delta = \pi/2$; · · ·, $k\delta = \pi$.

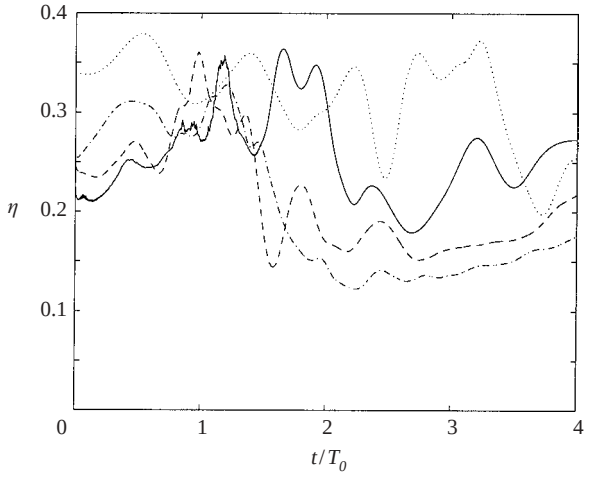

FIGURE 27. Instantaneous mixing efficiency η for four different interface thicknesses. —, $k\delta = \pi/10$; – – –, $k\delta = 3\pi/10$; —·—, $k\delta = \pi/2$; · · ·. $k\delta = \pi$.

The instantaneous relative rate of irreversible energy exchange is given by the instantaneous mixing efficiency (Winters *et al.* 1995)

$$\eta = \frac{\phi_d}{\phi_d + \epsilon}. \tag{5.8}$$

Figure 27 depicts the instantanous mixing efficiency for four different interface thicknesses up until $t/T_0 = 4$. The mixing efficiency after this point is not useful because as the dissipation vanishes, the mixing efficiency approaches unity and becomes irrelevant. From figure 27, we see that there is no apparent dependence of the maximum instantaneous mixing efficiency on the interface thickness. If the maximum dissipation increases, we would expect the mixing efficiency to decrease.

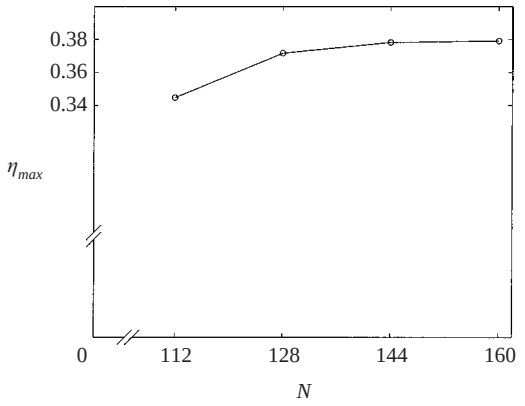

FIGURE 28. Maximum instantaneous mixing efficiency as a function of the number of cells in the horizontal, N, for a breaking interfacial wave with interface thickness $k\delta = \pi/10$. Each simulation is computed with N^3 total cells.

However, an increased dissipation is counteracted by an increased rate of change of the background potential energy, and hence, just like the bulk mixing efficiency, the instantaneous mixing efficiency is not affected by the interface thickness. The average maximum mixing efficiency for all the thicknesses is $\eta = 0.36 \pm 0.02$, bringing it to within the error bounds prescribed by the bulk mixing efficiency, $\eta_B = 0.42 \pm 0.07$. While the two values need not be equal, their statistical agreement shows that the bulk mixing efficiency is dominated by the peaks in the instantaneous mixing efficiency.

5.3. *Validation of the mixing efficiency*

We demonstrate that the result for the mixing efficiency is grid-independent by performing simulations of the breaking interfacial wave with $k\delta = \pi/10$ with varying grid resolution. With a total number of grid cells given by N^3, we plot the maximum instantaneous mixing efficiency as a function of the number of cells in the horizontal, N, in figure 28. This depicts the worst case scenario for convergence of the mixing efficiency, since it represents the thinnest interface case. Clearly, the mixing efficiency is converging to a value that is less than $\eta = 0.38$. The maximum mixing efficiency with $N = 128$ is given by $\eta = 0.378$, which is within 2% of the mixing efficiency for the most resolved case with $N = 160$. This indicates that the other calculations are at least as close to a converged value as this one, since convergence must improve with increased interface thickness. Therefore, the average mixing efficiency of $\eta = 0.36 \pm 0.02$ must be at least within 2% of the converged value, and represents a lower bound for the estimate of the mixing efficiency.

Table 1 depicts the mixing efficiency of several scenarios computed by other authors. The value we obtain for the mixing efficiency is consistent with the larger values obtained for convectively driven mixing induced by internal wave breaking. Breaking-wave experiments or simulations with lower values result from a predominant shear instability that governs the breaking, such as the interfacial wave breaking on slopes of Michallet & Ivey (1999) or the shear-induced breaking in critical layers of Lin *et al.* (1993). While there appears to be a correlation between the predominant instability and the mixing efficiency for breaking internal waves, it is important to note that this correlation only applies to the bulk mixing efficiency or the peak mixing efficiency computed during the turbulent phase of a breaking event. This is because the peak mixing efficiency can be extremely high during the preturbulent phase of a developing instability. For example, in their direct numerical simulations comparing

Mechanism	Reference	Mixing efficiency
Rayleigh–Taylor instability	Linden & Redondo (1991)	0.5
Breaking periodic interfacial waves	Present	0.36 ± 0.02
Critical topography	Slinn & Riley (1998*a*)	$0.32 - 0.38$
Standing waves	McEwan (1983*a*)	0.26 ± 0.06
Breaking interfacial waves on slopes	Michallet & Ivey (1999)	0.25
First principles	McEwan (1983*b*)	0.25
Critical layer	Dörnbrack (1998)	0.20
Critical layer	Lin *et al.* (1993)	0.13
Grid turbulence	Rehmann (1995)	0.05

TABLE 1. Mixing efficiencies computed by various authors.

Kelvin–Helmholtz to Holmboe instabilities, Smyth & Winters (2003) compute peak flux coefficients Γ_i of roughly 0.7 for the Kelvin–Helmholtz instability and in excess of unity for the Holmboe instability, which translate to mixing efficiencies of roughly $\eta = 0.41$ and $\eta = 0.5$, respectively, when using the approximation $\eta \approx \Gamma_i/(1 + \Gamma_i)$. These large values result from the extremely efficient nature of the flows in their preturbulent phases which result from a strong coherence of the laminar strain fields. As soon as the flows become turbulent, the instantaneous flux coefficients for both cases drop to their canonical values of 0.2. Therefore, we stress that the correlation between the mixing efficiency and the source of the instability can be made only during the turbulent or fully developed phases of a mixing event. That is, convectively driven turbulent mixing appears to be correlated with higher mixing efficiencies than shear-driven turbulent mixing, at least for breaking internal waves.

5.4. *Three-dimensionality*

In this section, we determine the importance of three-dimensional effects on the breaking dynamics. This is useful in determining whether or not two-dimensional simulations are suitable, and if not, how wide the domain must be made in the cross-stream dimension in order to perform accurate simulations while minimizing the computational expense. The three-dimensional nature of the flow can be quantified by computing the kinetic energy associated with each component of velocity in the three-dimensional simulations and comparing it to the two-dimensional simulations. The components of the kinetic energy are given by

$$E_1 = \frac{1}{2}\int_V u_1^2 \,\mathrm{d}V,$$
$$E_2 = \frac{1}{2}\int_V u_2^2 \,\mathrm{d}V,$$
$$E_3 = \frac{1}{2}\int_V u_3^2 \,\mathrm{d}V,$$

so that the total kinetic energy is given by $E_k = E_1 + E_2 + E_3$. The normalized departure from two-dimensionality of each component is given by

$$\Delta E_1 = \frac{E_{1,3} - E_{1,2}}{E_{k,3}},$$
$$\Delta E_2 = \frac{E_{2,3}}{E_{k,3}},$$

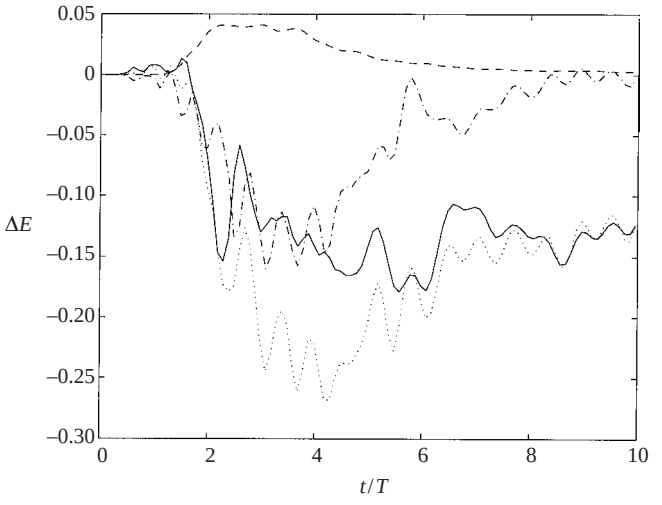

FIGURE 29. Normalized energy components quantifying the departure from two-dimensionality for a breaking interfacial wave with interface thickness $k\delta = 3\pi/5$. —, ΔE_1; – – –, ΔE_2; —·—, ΔE_3; · · · ΔE_k.

$$\Delta E_3 = \frac{E_{3,3} - E_{3,2}}{E_{k,3}},$$
$$\Delta E_k = \frac{E_{k,3} - E_{k,2}}{E_{k,3}},$$

where $E_{m,n}$ represents the mth component of energy in the nth dimensional computation. For example, $E_{1,3}$ represents the component of energy in the 1 direction for the 3 dimensional computation. $E_{k,n}$ represents the total kinetic energy of the nth dimensional computation. Therefore, the normalized departure from two-dimensionality represents a fraction of the total kinetic energy of the three-dimensional flow.

The departure from two-dimensionality for the interfacial wave with $k\delta = 3\pi/5$ is shown in figure 29. The figure shows that, while less than 5% of the three-dimensional energy is contained in the u_2-direction, the total kinetic energy of the three-dimensional flow is more than 25% less than that computed by the two-dimensional flow at $t/T = 4$. This is due to the lack of dissipation in the two-dimensional computation resulting from a lack of the three-dimensional longitudinal rolls. These rolls account for a significant portion of the dissipation in the three-dimensional computations. Figure 30 compares the two- and three-dimensional dissipation from (5.5) and rate of increase of the background potential energy from equation (5.3). In subplot (*a*), the rate of increase of the background potential energy is shown for both the two- and three-dimensional cases. Each is normalized by the maximum rate of increase for the three-dimensional case, $\phi_{d3,max}$. The same is done for subplot (*b*), where the dissipation for the two- and three-dimensional cases are normalized by the maximum dissipation for the three-dimensional case, $\epsilon_{3,max}$. While the peak rates of increase of the background potential energy do not differ substantially, the peak dissipation is roughly half as large for the two-dimensional case as it is for the three-dimensional case.

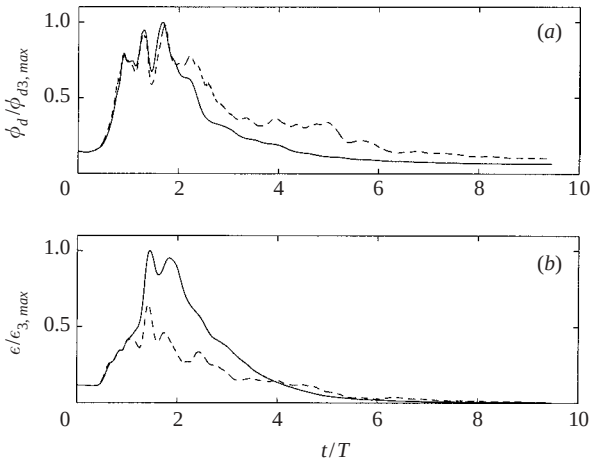

FIGURE 30. Rate of increase of (*a*) the background potential energy and (*b*) dissipation normalized by their maxima for the three-dimensional case for a breaking interfacial wave with interface thickness $k\delta = 3\pi/5$. —, three-dimensional computation; – – –, two-dimensional computation.

The rate of increase of the background potential energy is quite large for the two-dimensional case because of the reverse energy cascade of the two-dimensional turbulence. As a result of this energy cascade and the lack of three-dimensional longitudinal rolls, dissipation for the two-dimensional flow is substantially reduced, and the scales of motion become larger with time owing to two-dimensional vortex pairing. Owing to the relatively large Prandtl number of 7, the large vortices stretch out filaments of density and create grid-scale density variations in the flow field that cannot be resolved accurately by the SHARP scheme. As a result, the two-dimensional scalar advection scheme becomes highly diffusive. The three-dimensional flow does not suffer from this because the energy cascade is to smaller scales which are smeared by molecular viscosity. Large vortices do not form and thus grid-scale variations in density are minimized. Therefore, the density gradients in the three-dimensional case are still resolved accurately by the SHARP scheme and scalar diffusion resulting from numerical errors is minimal.

6. Conclusions

Finite-amplitude interfacial waves break as a result of an initial two-dimensional instability that leads to a three-dimensional convective instability. The initial two-dimensional instability can be divided into three regimes. The first regime concerns waves with $k\delta < 0.56$ and is covered by Troy (2003). In this regime, the most unstable wavelength associated with a shear instability is small enough to grow at the interface and develop Kelvin–Helmholtz billows, but it is not energetic enough to induce a two-dimensional convective instability within the wave. In the second regime, further increasing the interface thickness produces waves with energetic Kelvin–Helmholtz billows that induce a convective instability. The critical Richardson number during breaking in this regime is given by $Ri_{min} = 0.13$, indicating that interfacial waves can propagate stably with Richardson numbers less than the critical value of $Ri_{min} = 0.25$. In the last regime, waves having a non-dimensional interface thickness

that is greater than $k\delta = 2.33$ are limited in amplitude by a weak two-dimensional convective instability that results when $Fr_{max} > 1$.

Three-dimensional motions develop only after overturns are created as a result of the initial two-dimensional instability. The overturns induce a region of statically unstable fluid which is followed by a three-dimensional convective instability. This convective instability generates longitudinal rolls that account for roughly half of the dissipation when compared to the dissipation in the two-dimensional computations. Dissipation of wave energy is maximized when the steepness is the same as the non-dimensional interface thickness, or when $ka \sim k\delta$. The scale of the overturns in an interfacial wave with a thinner interface is too small to influence the overall character of the wave, and hence the result is localized mixing that thickens the interface without too much effect on the wave amplitude. On the other hand, waves with a non-dimensional interface thickness that is greater than the steepness contain weak two-dimensional convective billows that are also not energetic enough to cause significant dissipation and mixing. Instead, the larger motions develop wave components that introduce an oscillatory character to the wave, and through nonlinear interactions, induce sporatic breaking after the initial breaking event.

Upon wave breaking, the background potential energy rises irreversibly and the available potential energy is lost irreversibly to viscosity. The efficiency with which the breaking process mixes the density field is calculated in one of two ways. The first is calculated by computing the changes in available and background potential energy before and after wave breaking, and using these to compute a mixing efficiency. This bulk mixing efficiency is estimated to be $\eta_B = 0.42 \pm 0.07$ and is a weak function of the interface thickness. The second method of computing the mixing efficiency is by using the instantaneous rate of increase of the background potential energy and the instantaneous dissipation. The maximum instantaneous mixing efficiency is given by $\eta = 0.36 \pm 0.02$, and it is also weakly dependent upon the interface thickness. Compared with other values in the literature which are computed for turbulent mixing events, the maximum instantaneous mixing efficiency is quite large, indicating that the turbulent mixing is convectively driven.

O. B. F. acknowledges his support as a Computational Science Graduate Fellow, DOE. R. L. S. acknowledges support of ONR Grant N0014-99-1-0413 (Scientific Officer: Dr Stephen Murray, Physical Oceanography Program). The authors also acknowledge Cary Troy, Steve Armfield, Jeff Koseff and Greg Ivey for their invaluable comments and suggestions. Simulations were carried out at the Peter A. McCuen Environmental Computing Center at Stanford University.

Appendix. Modal analysis

This appendix outlines the methodology used to obtain the linearized wave frequency ω given an interface thickness $k\delta$.

A.1. *Non-dimensional Sturm–Liouville problem*

The linearized non-hydrostatic equations of motion within a two-dimensional stratified fluid are given by

$$\frac{\partial u}{\partial t} = -\frac{1}{\rho_0}\frac{\partial p}{\partial x}, \tag{A 1}$$

$$\frac{\partial w}{\partial t} = -\frac{1}{\rho_0}\frac{\partial p}{\partial z} - \frac{\rho}{\rho_0}g, \tag{A 2}$$

$$\frac{\partial \rho}{\partial t} = \frac{\rho_0 N^2}{g} w, \tag{A 3}$$

$$\frac{\partial u}{\partial x} + \frac{\partial w}{\partial z} = 0, \tag{A 4}$$

where all quantities represent perturbations from a state of rest in which the background density profile is used to define the buoyancy frequency as

$$N^2 = -\frac{g}{\rho_0} \frac{\mathrm{d}\overline{\rho}}{\mathrm{d}z}. \tag{A 5}$$

Solving for w in the linearized equations of motion yields

$$\frac{\partial^2}{\partial t^2} \left(\frac{\partial^2 w}{\partial x^2} + \frac{\partial^2 w}{\partial z^2} \right) + N^2 \frac{\partial^2 w}{\partial x^2} = 0. \tag{A 6}$$

Assuming a modal decomposition of the form

$$w = \sum_{n=0}^{\infty} w_n \Psi_n(z), \tag{A 7}$$

where $w_n = \hat{w}_n \exp(i(k_n x - \omega_n t))$, and substitution of w into equation (A 6) results in the eigenvalue problem

$$\frac{1}{\left(N^2 - \omega_n^2\right)} \frac{\mathrm{d}^2 \Psi_n}{\mathrm{d}z^2} + \frac{1}{c_n^2} \Psi_n = 0, \tag{A 8}$$

where each eigenfunction Ψ_n propagates at the the speed $c_n = \omega_n / k_n$. The boundary conditions on equation (A 8) require that

$$\Psi_n = 0 \quad z = 0, -d, \tag{A 9}$$

in order to satisfy the no-flux boundary condition at the upper and lower boundaries. It is acceptable to require that both the horizontal and vertical velocities vanish at $z = 0$ and $z = -d$ since we will assume *a priori* that the modes propagate as deep-water waves and are not affected by the upper and lower boundaries of the domain.

The initial non-dimensional density profile in the simulations is given by

$$\overline{\rho}'(z') = \tfrac{1}{2} \tanh \left[2 \frac{kd}{k\delta} \tanh^{-1} \alpha \left(z' - \tfrac{1}{2} \right) \right], \tag{A 10}$$

where $\overline{\rho}' = \overline{\rho} / \Delta\rho$, $z' = z/d$ and $\alpha = 0.99$. Defining $\omega_n = N_0 \omega_n'$ and $N = N_0 N'$, where $N_0^2 = g/d$, the non-dimensional Brunt–Väissälä frequency becomes

$$(N')^2 = -\frac{\Delta\rho}{\rho_0} \frac{\mathrm{d}\overline{\rho}'}{\mathrm{d}z'}. \tag{A 11}$$

The ordinary differential equation (A 8) along with the boundary conditions (A 9) can then be non-dimensionalized so that the non-dimensional Sturm–Liouville problem becomes

$$\frac{1}{\left(N^2 - \omega_n^2\right)} \frac{\partial^2 \Psi_n}{\partial z^2} + \lambda_n \Psi_n = 0 \tag{A 12}$$

$$\Psi_n = 0, \quad z = 0, -1, \tag{A 13}$$

where $\lambda_n^{1/2} = d N_0 / c_n$, and the primes have been omitted for clarity.

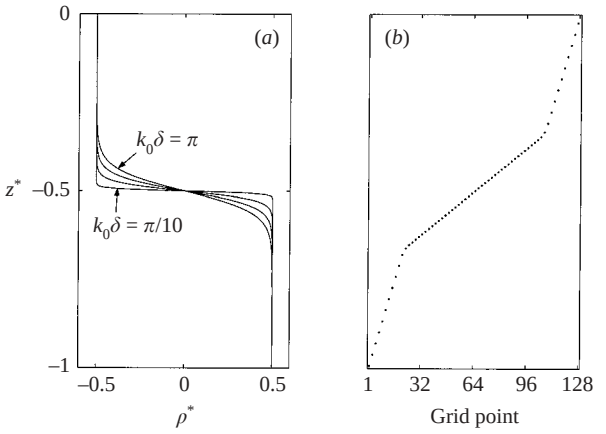

FIGURE 31. (*a*) Density and (*b*) grid distributions used to solve the Sturm–Liouville problem (A 12) for $k_0\delta = \pi/10$, $2\pi/5$, $7\pi/10$, and π. Every other grid point is shown for clarity.

A.2. *Numerical solution*

The Sturm–Liouville problem is discretized with a second-order centred finite-difference discretization on an arbitrarily spaced mesh such that the discretized form of equation (A 12) is given by the tridiagonal system

$$A_i\psi_{i-1} + B_i\psi_i + C_i\psi_{i+1} - \lambda_n\psi_i = 0, \tag{A 14}$$

in which the coefficents are given by

$$\begin{aligned} A_i &= -\frac{2}{\left(N_i^2 - \omega_n^2\right)(z_{i+1} - z_{i-1})(z_i - z_{i-1})}, \\ B_i &= \frac{2}{\left(N_i^2 - \omega_n^2\right)(z_{i+1} - z_{i-1})}\left(\frac{1}{z_{i+1} - z_i} + \frac{1}{z_i - z_{i-1}}\right), \\ C_i &= -\frac{2}{\left(N_i^2 - \omega_n^2\right)(z_{i+1} - z_{i-1})(z_{i+1} - z_i)}, \end{aligned} \tag{A 15}$$

for $i = 2, \ldots, M_i - 1$, where M_i is the number of points discretizing the domain, including ghost points. Applying the boundary conditions (A 13) results in

$$\begin{aligned} B_2 &\rightarrow B_2 - A_2, \\ B_{M_i-1} &\rightarrow B_{M_i-1} - C_{M_i-1}. \end{aligned}$$

The ψ_i which satisfy equation (A 14) then solve the eigenvalue problem for the real tridiagonal non-symmetric matrix $\boldsymbol{A} \in \Re^{(M_i-2)\times(M_i-2)}$,

$$(\boldsymbol{A} - \lambda_n\boldsymbol{I})\Psi_n = 0, \tag{A 16}$$

where $\Psi_n = [\psi_2, \psi_3, \ldots, \psi_{M_i-1}] \in \Re^{M_i-2}$ is the nth eigenvector corresponding to the eigenvalue λ_n. Since we are interested in the first, or fastest, mode, this corresponds to the smallest eigenvalue of $\boldsymbol{A}$, or λ_0.

In general, given a wavenumber k_0, we would like to obtain the first mode eigenvalue λ_0 to determine the frequency ω_0 or phase speed c_0. Therefore, a Newton iteration is required. With $k_0 d = 3\pi$, we iterate to obtain the eigenvalue λ_0 for $k_0\delta = m\pi/10$, where $m = [1, \ldots, 10]$. The density fields are shown in figure 31(*a*), and the 128-point grid we use to discretize the equations is shown in figure 31(*b*). Figure 32(*a*) depicts the

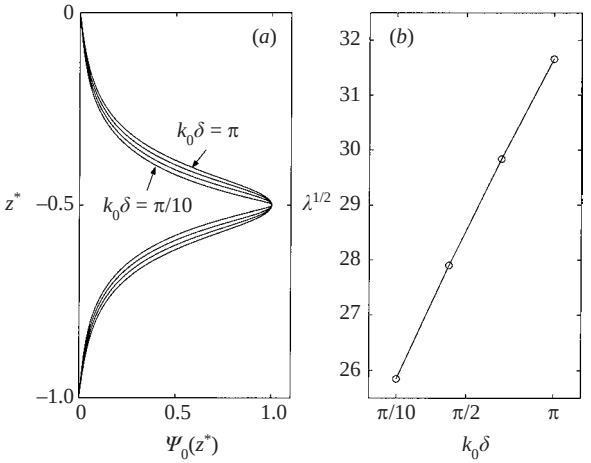

FIGURE 32. (*a*) First mode solution Ψ_0 to the non-dimensional Sturm–Liouville problem (A 12) and (*b*) its associated minimum eigenvalue $\lambda_0^{1/2}$ for $k_0\delta = \pi/10$, $2\pi/5$, $7\pi/10$ and π.

first mode solution Ψ_0 for each $k_0\delta$, corresponding to the minimum eigenvalue $\lambda_0^{1/2}$, shown in figure 32(*b*).

REFERENCES

ARMFIELD, S. W. & STREET, R. L. 2000 Fractional step methods for the Navier-Stokes equations on non-staggered grids. *ANZIAM J.* **42(E)**, C134–C156.

BAKER, B. R., MEIRON, D. I. & ORSZAG, S. A. 1982 Generalized vortex methods for free-surface flow problems. *J. Fluid Mech.* **123**, 477–501.

CHEN, G., KHARIF, C., ZALESKI, S. & LI, J. 1999 Two-dimensional Navier–Stokes simulation of breaking waves. *Phys. Fluids* **11**, 121–133.

COKELET, E. D. 1977 Breaking waves. *Nature* **267**, 769–774.

DÖRNBRACK, A. 1998 Turbulent mixing by breaking gravity waves. *J. Fluid Mech.* **375**, 113–141.

DÖRNBRACK, A. & GERZ, T. 1995 Generation of turbulence by overturning gravity waves below a critical level. In *Proc. 11th Symposium on Boundary Layers and Turbulence*, pp. 576–579. American Meteorological Society.

DRAZIN, P. G. 1977 On the instability of an internal gravity wave. *Proc. R. Soc. Lond.* A **356**, 411–432.

FRINGER, O. B. 2003 Numerical simulations of breaking interfacial waves. PhD dissertation, Stanford University.

HARLOW, F. H. & WELCH, J. E. 1965 Numerical calculation of time-dependent viscous incompressible flow of a fluid with free surface. *Phys. Fluids* **8**, 2182–2189.

HAZEL, P. 1972 Numerical studies of the stability of inviscid stratified shear flows. *J. Fluid Mech.* **51**, 39–61.

HODGES, B. R. & STREET, R. L. 1999 On simulation of turbulent nonlinear free-surface flows. *J. Comput. Phys.* **151**, 425–457.

HOLYER, J. Y. 1979 Large amplitude progressive interfacial waves. *J. Fluid Mech.* **93**, 433–448.

IVEY, G. N. & IMBERGER, J. 1991 On the nature of turbulence in a stratified fluid. Part I: The energetics of mixing. *J. Phys. Oceanogr.* **21**, 650–658.

JOU, W. & WEISSMAN, M. A. 1987 A perturbation solution for long internal waves. *Phys. Fluids* **30**, 1699–1707.

LEONARD, B. P. 1979 A stable and accurate convective modelling procedure based on quadratic upstream interpolation. *Comput. Meth. Appl. Mech.* **19**, 59–98.

Leonard, B. P. 1987 Sharp simulation of discontinuities in highly convective steady flow. *NASA Techn. Mem.* 100240.

Lin, C. L., Ferziger, J. H., Koseff, J. R. & Monismith, S. G. 1993 Simulation and stability of two-dimensional internal gravity waves in a stratified shear flow. *Dyn. Atmos. Oceans* **19**, 325–366.

Linden, P. F. & Redondo, J. J. 1991 Molecular mixing in Rayleigh–Taylor instability. *Phys. Fluids* A **3**, 1269–1277.

McEwan, A. D. 1983*a* Internal mixing in stratified fluids. *J. Fluid Mech.* **128**, 59–80.

McEwan, A. D. 1983*b* The kinematics of stratified mixing through internal wave breaking. *J. Fluid Mech.* **128**, 47–48.

Meiron, D. I. & Saffman, P. G. 1983 Overhanging interfacial gravity waves of large amplitude. *J. Fluid Mech.* **129**, 213–218.

Michallet, H. & Ivey, G. N. 1999 Experiments on mixing due to internal solitary waves breaking on uniform slopes. *J. Geophys. Res.* **104**, 13,467–13,477.

Munk, W. & Wunsch, C. 1998 Abyssal recipes II: energetics of tidal and wind mixing. *Deep-Sea Res.* **45**, 1977–2010.

Petruncio, E. T., Rosenfeld, L. K. & Paduan, J. D. 1998 Observations of the internal tide in Monterey Canyon. *J. Phys. Oceanogr.* **28**, 1873–1903.

Phillips, O. M. 1977 *The Dynamics of the Upper Ocean*. Cambridge University Press.

Puckett, E. G., Almgren, A. S., Bell, J. B., Marcus, D. L. & Rider, W. J. 1997 A high-order projection method for tracking fluid interfaces in variable density incompressible flows. *J. Comput. Phys.* **130**, 269–282.

Rehmann, C. R. 1995 Effects of stratification and molecular diffusivity on the mixing efficiency of decaying grid turbulence. PhD dissertation, Stanford University.

Roberts, E. S. 1998 *Programming Abstractions in C*. Addison-Wesley.

Rosenfeld, L. & Kunze, E. 1998 Internal waves in Monterey Canyon. *Coastal Ocean Processes Symp., Woods Hole, MA, Woods Hole Oceanographic Institution.* Extended abstracts.

Slinn, D. N. & Riley, J. J. 1998*a* Turbulent dynamics of a critically reflecting internal gravity wave. *Theor. Comput. Fluid Dyn.* **11**, 281–303.

Slinn, D. N. & Riley, J. J. 1998*b* A model for the simulation of turbulent boundary layers in an incompressible stratified flow. *J. Comput. Phys.* **144**, 550–602.

Smyth, W. D. & Winters, K. B. 2003 Turbulence and mixing in Holmboe waves. *J. Phys. Oceanogr.* **33**, 694–711.

Stanton, T. P. & Ostrovsky, L. A. 1998 Observations of highly nonlinear interal solitons over the continental shelf. *Geophys. Res. Lett.* **25**, 2695–2698.

Stokes, G. G. 1880 Considerations relative to the greatest height of oscillatory irrotational waves. *Mathematical and Physical Papers,* vol. 1, pp. 225–228. Cambridge University Press.

Thompson, R. O. R. Y. 1980 Efficiency of conversion of kinetic energy to potential energy by a breaking internal gravity wave. *J. Geophys. Res.* **85**, 6631–6635.

Thorpe, S. A. 1978 On the shape and breaking of finite amplitude internal gravity waves in a shear flow. *J. Fluid Mech.* **85**, 7–31.

Troy, C. D. 2003 The breaking and mixing of interfacial waves. PhD dissertation, Stanford University.

Tsugi, Y. & Nagata, Y. 1973 Stokes' expansion of internal deep water waves to the fifth order. *J. Oceanogr. Soc. Japan* **29**, 61–69.

Winters, K. B. & D'Asaro, E. A. 1989 Two-dimensional instability of finite amplitude internal gravity wave packets near a critical level. *J. Geophys. Res.* **94**, 12,709–12,719.

Winters, K. B. & D'Asaro, E. A. 1994 Three-dimensional wave instability near a critical level. *J. Fluid Mech.* **272**, 255–284.

Winters, K. B., Lombard, P. N., Riley, J. J. & D'Asaro, E. A. 1995 Available potential energy and mixing in density-stratified flows. *J. Fluid Mech.* **289**, 115–128.

Winters, K. B. & Riley, J. J. 1992 Instability of internal waves near a critical level. *Dyn. Atmos. Oceans* **16**, 249–278.

Zang, Y., Street, R. L. & Koseff, J. R. 1994 A non-staggered grid, fractional step method for time-dependent incompressible Navier–Stokes equations in curvilinear coordinates. *J. Comput. Phys.* **114**, 18–33.